Quantum-Switch-Assisted Teleportation of Quantum Fisher Information under Composite Pauli Channels

Yan-Ling Li[1,2], Jiani Luo[1], and Xing Xiao[3]*
[1] School of Information Engineering, Jiangxi University of Science and Technology, Ganzhou, Jiangxi 341000, China
[2] Jiangxi Provincial Key Laboratory of Multidimensional Intelligent Perception and Control, Jiangxi University of Science and Technology, Ganzhou, 341000, China
[3] School of Physics and Electronic Information, Gannan Normal University, Ganzhou, Jiangxi 341000, China
(Dated: September 24, 2026)

The teleportation of Quantum Fisher Information (QFI) is central to the precision limits of distributed quantum metrology, yet it is inevitably degraded by environmental decoherence. Here we investigate QFI teleportation under composite Pauli channels and show that a quantum switch can improve the outcome-resolved and success-probability-weighted QFI relative to the corresponding fixed-order protocol. The enhancement arises from a coherent reorganization of Pauli error trajectories rather than from a reduction of the physical error probabilities. For the three binary pairs of anti-commuting Pauli channels studied here, we identify a heralded branch whose normalized state has the ideal QFI whenever that branch has nonzero probability. These findings highlight the potential of utilizing quantum switches to mitigate Pauli-noise-induced QFI degradation in quantum communication and sensing networks.

PACS numbers: 03.67.–a, 42.50.Lc
Keywords: quantum Fisher information, quantum teleportation, indefinite causal order, Pauli channels

I. INTRODUCTION

Quantum teleportation is a well-known protocol in quantum information science that enables the transfer of an unknown quantum state between distant parties using shared entanglement and classical communication [1–4]. Since its original proposal, the performance of quantum teleportation has been characterized by state-based metrics, most notably the fidelity between the input and reconstructed states. In many emerging quantum technologies, however, the figure of merit is not the faithful recovery of the entire quantum state, but rather the physical information encoded within it. This perspective is especially relevant to quantum metrology [5–7], where quantum states serve as carriers of unknown parameters and the achievable estimation precision is determined by the amount of parameter information preserved during transmission. Quantum Fisher information (QFI) [8, 9] is the fundamental measure of parameter sensitivity: it quantifies the ultimate precision limit allowed by quantum mechanics. QFI plays a central role in applications ranging from quantum metrology [10, 11], distributed quantum sensing [12–14], quantum imaging [15, 16], and quantum gravitational detection [17, 18]. Therefore, beyond conventional state teleportation, the teleportation and preservation of QFI represent a more practical task, where maintaining the encoded metrological information becomes more crucial than preserving the state fidelity.

However, quantum channels inevitably introduce decoherence [19], leading to degradation of QFI during teleportation and limiting the achievable precision in parameter estimation [20, 21]. Various strategies have been developed to mitigate the detrimental effects of noise in quantum systems [22–27]. Dynamical decoupling, for instance, suppresses decoherence by applying external control pulses that average out unwanted system-environment interactions; it is particularly effective against dephasing and slowly fluctuating noise [28–30]. Quantum error correction provides a more general framework by encoding quantum information into protected subspaces, although this approach usually demands substantial additional physical resources and operational overhead [31, 32]. Recently, weak measurement and its reversal (WMMR) have emerged as promising approaches for suppressing amplitude damping noise. These techniques can probabilistically recover lost quantum entanglement [33–35], QFI [36, 37] and teleportation fidelity [38–40]. Despite these advances, existing techniques tend to be effective only against specific noise structures or at the cost of additional control resources. In realistic quantum communication platforms, Pauli-type decoherence remains one of the most prevalent error mechanisms [41, 42], affecting systems such as photon polarization systems [43, 44], superconducting circuits [45, 46], and other qubit-based architectures. In such scenarios, information carriers usually experience sequential Pauli channels with a definite causal order, where the accumulation of multiple noise processes becomes unavoidable and leads to progressive degradation of quantum resources.

Unlike the above approaches, which manipulate the system-environment interaction or encode information into protected subspaces, indefinite causal order (ICO) offers a different strategy: it controls noisy quantum processes by modifying the causal structure of quantum operations [47–50]. In conventional quantum information protocols, quantum channels are assumed to act in a def-

* xiaoxing@gnnu.edu.cn

inite temporal sequence, where one operation must precede another. In contrast, ICO allows different causal orders of quantum operations to exist in a coherent superposition. A representative realization of ICO is the quantum switch [51], where an auxiliary control qubit determines the order in which two quantum channels are applied. When the control qubit is prepared in a superposition state, the target system simultaneously experiences alternative evolutions corresponding to different channel orders, enabling a coherent combination of processes such as $\mathcal{E}_1 \circ \mathcal{E}_2$ and $\mathcal{E}_2 \circ \mathcal{E}_1$.

The quantum switch has demonstrated a series of counterintuitive advantages in quantum information processing [52–57]. It has been shown to enhance communication performance by increasing achievable channel capacities and improving information transmission through noisy environments [55, 58, 59]. Remarkably, the quantum switch can activate communication through channels that are individually incapable of transmitting information, for instance, enabling transmission through zero-capacity channels [60–62]. Beyond communication, quantum switches have also demonstrated advantages in channel and state discrimination [63, 64], quantum parameter estimation [65–68], entanglement distribution [69], and quantum gate teleportation [70]. These results indicate that the superposition of causal orders provides a mechanism for manipulating quantum processes that is qualitatively distinct from conventional approaches based on fixed causal structures. In this paradigm, the causal structure itself becomes a quantum degree of freedom, opening new possibilities for controlling decoherence and protecting quantum resources in quantum information tasks.

Although quantum switches have demonstrated advantages in quantum communication and state transmission, their ability to protect metrological information, quantified by QFI, in distributed teleportation scenarios has received much less attention. In this work, we investigate quantum-switch-assisted teleportation of QFI under composite Pauli noise, as shown in Fig. 1(a). By deriving analytical expressions for the output states and the corresponding QFI under single- and dual-switch configurations, we show that the switch can provide a higher outcome-resolved, success-probability-weighted QFI than the corresponding fixed-order protocols for the three representative binary channel pairs considered here. For specific control outcomes (the $|-\rangle$ branch in the single-switch case and the $|--\rangle$ branch in the dual-switch case), the conditional teleported state has the ideal QFI and is related to the ideal input by a unitary operation whenever the selected branch has nonzero probability. The unitary correction conditioned on the herald is deterministic, whereas the herald itself occurs with probability Q_- (or Q_{--}). The enhancement originates from a coherent reorganization of Pauli error trajectories, not from a reduction of their physical probabilities. Finally, we propose a verification scheme based on a linear-optical photonic platform.

The present quantum-switch protocol instead leaves the two channel maps unchanged and coherently controls their order. For the three binary models studied here, the nonzero commutator sector contains one known Pauli operation, so the switch provides a control-tagged, exactly correctable branch without redundant logical encoding or measurement-strength optimization. The resource reduction relative to full QEC is obtained at the cost of a path/control degree of freedom per independently switched arm, coherent access to both orders, interferometric stabilization, control readout, and feedforward.

The remainder of this paper is organized as follows. In Sec. II, we introduce the theoretical preliminaries, including QFI and the quantum switch. In Sec. III, we study single-switch-assisted teleportation of QFI under composite Pauli channels and compare its performance with conventional fixed-order protocols. In Sec. IV, we further extend the protocol to distributed QFI teleportation using dual quantum switches. In Sec. V, we present a discussion of the underlying causal-reorganization mechanism. An experimental verification scheme is proposed in Sec. VI. Finally, Sec. VII summarizes the main conclusions and discusses possible future developments.

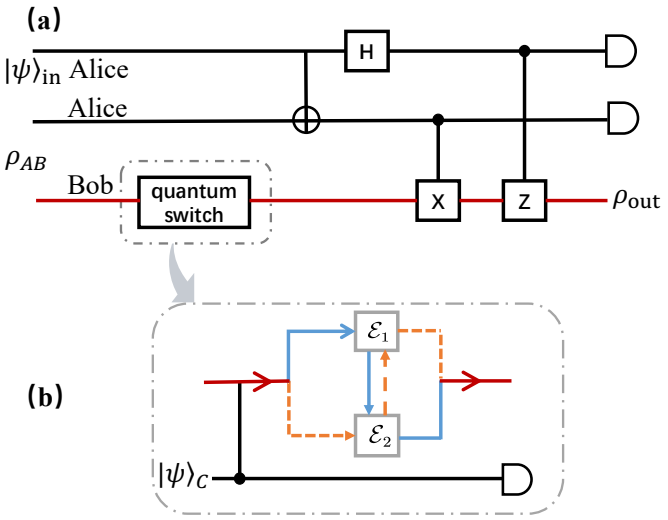


FIG. 1: Schematic illustrations of quantum-switch-assisted QFI teleportation. (a) In the single-switch protocol, the photon sent to Bob is subjected to two Pauli channels $\mathcal{E}_1$ and $\mathcal{E}_2$, whose order is coherently controlled. (b) An auxiliary qubit prepared in $|\psi\rangle_C = (|0\rangle + |1\rangle)/\sqrt{2}$ coherently controls the orders $\mathcal{E}_2 \circ \mathcal{E}_1$ and $\mathcal{E}_1 \circ \mathcal{E}_2$.

II. THEORETICAL PRELIMINARIES

In this section we briefly review the two conceptual pillars of this work: QFI and the quantum switch.

A. QFI

QFI quantifies the ultimate precision achievable when estimating a parameter encoded in a quantum state. Unlike classical Fisher information, which is tied to a specific measurement, QFI is obtained by maximizing the classical Fisher information over all possible positive operator-valued measures (POVMs). For any unbiased estimator, the variance of the estimate is bounded from below by the quantum Cramér–Rao bound [71]:

$$\Delta^2\phi \geq \frac{1}{N\mathcal{F}_\phi}, \tag{1}$$

where N denotes the number of independent measurements and $\mathcal{F}_\phi$ is the QFI with respect to the parameter ϕ. Preserving QFI during quantum information processing is therefore central to high-precision quantum sensing and distributed metrology.

For a parameter-dependent density matrix ρ_ϕ, the QFI is defined via the symmetric logarithmic derivative (SLD) operator L_ϕ, which satisfies $\frac{\partial\rho_\phi}{\partial\phi} = \frac{1}{2}(L_\phi\rho_\phi + \rho_\phi L_\phi)$. The QFI is then given by $\mathcal{F}_\phi = \mathrm{Tr}\left(\rho_\phi L_\phi^2\right)$. Using the spectral decomposition $\rho_\phi = \sum_i \lambda_i|i\rangle\langle i|$, the QFI can be explicitly calculated as [72, 73]

$$\mathcal{F}_\phi = 2\sum_{i,j}\frac{\left|\langle i|\partial_\phi\rho_\phi|j\rangle\right|^2}{\lambda_i+\lambda_j}, \tag{2}$$

where the sum runs only over terms with $\lambda_i + \lambda_j > 0$.

For a single-qubit system, the density matrix can be parameterized by the Bloch vector $\boldsymbol{\omega} = (\omega_x, \omega_y, \omega_z)^T$ as

$$\rho_\phi = \frac{1}{2}\left(I + \boldsymbol{\omega}\cdot\boldsymbol{\sigma}\right), \tag{3}$$

where $\boldsymbol{\sigma} = (\sigma_x, \sigma_y, \sigma_z)$ is the vector of Pauli matrices. In this representation, the QFI takes the compact form [74, 75]:

$$\mathcal{F}_\phi = \begin{cases} |\partial_\phi\boldsymbol{\omega}|^2, & \text{if } |\boldsymbol{\omega}| = 1, \\ |\partial_\phi\boldsymbol{\omega}|^2 + \frac{(\boldsymbol{\omega}\cdot\partial_\phi\boldsymbol{\omega})^2}{1-|\boldsymbol{\omega}|^2}, & \text{if } |\boldsymbol{\omega}| < 1. \end{cases} \tag{4}$$

For $|\boldsymbol{\omega}| = 1$ the state is pure and the second term vanishes; for $|\boldsymbol{\omega}| < 1$ the additional term accounts for the contribution of the state's mixedness to the accessible information. We employ this Bloch-vector formalism throughout the paper to evaluate the QFI of teleported states after transmission through noisy quantum channels. For notational simplicity, we omit the subscript ϕ in what follows.

B. Quantum Switch

In conventional quantum information processing, quantum operations follow a fixed causal structure, with their temporal order specified in advance. For two quantum channels, the evolution is restricted to either $\mathcal{E}_2\circ\mathcal{E}_1$ or $\mathcal{E}_1\circ\mathcal{E}_2$. As a result, when a quantum state passes sequentially through several noisy channels, decoherence accumulates according to the fixed channel order; there is no freedom to control noise propagation beyond the choice of the sequence itself.

ICO allows different orders of quantum operations to coexist in a coherent superposition rather than in a classical probabilistic mixture. The quantum switch provides a physical realization of this idea [51]: an auxiliary control qubit coherently determines the order in which two quantum channels are applied. The causal structure is therefore promoted from a fixed background to a controllable degree of freedom.

To illustrate this mechanism, we consider two quantum channels $\mathcal{E}_1$ and $\mathcal{E}_2$ with Kraus operators $E_i^{(1)}$ and $E_j^{(2)}$, respectively. As shown in Fig. 1(b), the quantum switch employs a control qubit whose state coherently determines the order of the two channels. When the control qubit is prepared in the state $|0\rangle$, the target system undergoes the sequence $\mathcal{E}_2\circ\mathcal{E}_1$, whereas $|1\rangle$ corresponds to the reverse order $\mathcal{E}_1\circ\mathcal{E}_2$. When the control qubit is initialized in the superposition state

$$|+\rangle_C = \frac{|0\rangle + |1\rangle}{\sqrt{2}}, \tag{5}$$

the target system simultaneously experiences both orders in a coherent superposition. The resulting evolution is a coherent superposition of the two causal sequences, not a classical mixture of the two. This coherent control of causal order distinguishes the quantum switch from conventional noise-control methods based on modifying channel parameters or system dynamics.

Formally, the quantum switch is a higher-order quantum transformation. It is a supermap that takes quantum channels as input and produces a new effective channel [76, 77]. For an input state ρ and a control state ρ_C, the output state is

$$S(\mathcal{E}_1,\mathcal{E}_2)(\rho\otimes\rho_C) = \sum_{ij} W_{ij}(\rho\otimes\rho_C)W_{ij}^\dagger, \tag{6}$$

where W_{ij} are the Kraus operators of the effective channel induced by the quantum switch on the joint target-control system, given by

$$W_{ij} = E_{2j}E_{1i}\otimes|0\rangle_C\langle 0| + E_{1i}E_{2j}\otimes|1\rangle_C\langle 1|. \tag{7}$$

Here, E_{1i} and E_{2j} are Kraus operators of $\mathcal{E}_1$ and $\mathcal{E}_2$, respectively. The expression in Eq. (7) shows that the control degree of freedom coherently combines the two causal sequences. For Pauli channels, the two measurement outcomes of the control qubit separate commuting and anti-commuting error trajectories. This separation forms the physical basis of the QFI enhancement, which will be discussed in Sec. V in detail.

III. QUANTUM SWITCH ENHANCES QFI TELEPORTATION UNDER COMPOSITE PAULI NOISE

Pauli channels provide an effective description when the physical process is Pauli diagonal or when an explicit twirling operation is justified. We assume that both Pauli channels $\mathcal{E}_1$ and $\mathcal{E}_2$ are given in Kraus forms [78]:

$$E_{mk} = \sqrt{p_{mk}}\sigma_k \quad m = 1, 2, \quad k = 0, 1, 2, 3, \tag{8}$$

where $\sigma_0 = I$, $\sigma_1 = X$, $\sigma_2 = Y$, $\sigma_3 = Z$ denote the identity and three Pauli operators, respectively. The coefficient p_{mk} represents the probability associated with the k-th Pauli error on the m-th channel with $\sum_k p_{mk} = 1$ for each m.

For clarity, p_{mk} is an error probability, not a parameter that measures decoherence monotonically over its full interval. For a binary Pauli channel

$$\mathcal{E}_P^{(p)}(\rho) = (1-p)\rho + pP\rho P, \tag{9}$$

the Bloch components perpendicular to P are multiplied by $1-2p$. The stochastic mixing is maximal at $p = 1/2$, whereas $p = 1$ is the deterministic and reversible unitary operation P.

The three pairs $X+Y$, $X+Z$, and $Y+Z$ are algebraic benchmark cases spanning the three pairs of orthogonal Pauli axes; each notation describes two sequential binary channels, not one microscopic fiber process. With $|0\rangle = |H\rangle$ and $|1\rangle = |V\rangle$, X swaps $|H\rangle$ and $|V\rangle$, Z applies their relative phase, and Y combines a swap with a relative $\pm i$ phase. A realistic birefringent fiber more generally produces the time- and frequency-dependent rotation

$$U(\omega, t) = \exp\left[-\frac{i}{2}\delta(\omega, t)\,\hat{\boldsymbol{n}}(\omega, t)\cdot\boldsymbol{\sigma}\right], \tag{10}$$

rather than a discrete Pauli flip. Slow temperature and mechanical perturbations change the retardance δ and the birefringent axis $\hat{\boldsymbol{n}}$, generating polarization drift [79, 80]. For a nearly fixed principal axis, removal of the mean rotation followed by ensemble averaging over unresolved retardance fluctuations gives a dephasing channel [81].

An experimentally reconstructed polarization channel can be written as

$$\mathcal{E}_{\text{fib}}(\rho) = \sum_{\mu,\nu=0}^{3} \chi_{\mu\nu}\sigma_\mu\rho\sigma_\nu. \tag{11}$$

After alignment with the principal axes and ensemble averaging, an approximately diagonal χ reduces to a Pauli channel. Two approximately independent, Pauli-diagonal stages with different dominant axes can motivate the composite pairs studied here.

In practical quantum communication networks, transmitted quantum states rarely experience a single isolated error process. Instead, they may undergo a sequence of different Pauli errors originating from multiple propagation stages, imperfect local operations, or interactions with heterogeneous environments. Such scenarios lead to composite Pauli noise, in which several independent Pauli errors act successively on the same quantum system. As we will show, when these channels operate with a fixed causal order, the accumulated decoherence can accelerate the degradation of both entanglement and QFI.

A. QFI Teleportation under Fixed Causal Order

Before investigating the advantage of ICO for QFI teleportation, we first establish the baseline: QFI teleportation under a conventional fixed causal structure. We assume the parameter ϕ is encoded in the initial state

$$|\psi\rangle_{\text{in}} = \cos\frac{\theta}{2}|0\rangle + e^{i\phi}\sin\frac{\theta}{2}|1\rangle. \tag{12}$$

Alice prepares a maximally entangled resource state

$$\rho_{AB} = |\Phi^+\rangle_{AB}\langle\Phi^+|, \tag{13}$$

where $|\Phi^+\rangle_{AB} = (|00\rangle + |11\rangle)/\sqrt{2}$ is the Bell state. One particle of the entangled pair is transmitted from Alice to Bob through the noisy quantum channel. We assume that the transmitted particle experiences two Pauli channels, $\mathcal{E}_1$ and $\mathcal{E}_2$. Under a fixed causal order, the overall evolution is described by the channel composition $\mathcal{E}_2 \circ \mathcal{E}_1(\rho_{AB})$. For the independent Pauli channels considered here, the sequential composition $\mathcal{E}_2 \circ \mathcal{E}_1$ and $\mathcal{E}_1 \circ \mathcal{E}_2$ produce identical effective channels, i.e., $\mathcal{E}_2 \circ \mathcal{E}_1\left(\rho_{AB}\right) = \mathcal{E}_1 \circ \mathcal{E}_2\left(\rho_{AB}\right)$. This invariance reflects the absence of causal control in the fixed-order framework.

The shared state after transmission through the noisy channels is

$$\rho_{AB}^{\text{fo}} = \sum_{i,j=0}^{3} E_{2j}^B\, E_{1i}^B \rho_{AB} \left(E_{1i}^B\right)^\dagger \left(E_{2j}^B\right)^\dagger, \tag{14}$$

where the superscript "fo" stands for fixed order. Here, $E_{k,i}^B = I^{(A)} \otimes E_{k,i}^{(B)}$ $(k = 1, 2)$ represent the composite Kraus operators associated with particle B, which undergoes noisy channels $\mathcal{E}_1$ and $\mathcal{E}_2$, respectively, while particle A remains noise-free.

Substituting Eq. (8) into Eq. (14) yields the compact form

$$\rho_{AB}^{\text{fo}} = \sum_{i=0}^{3}(a_i + b_i)(I \otimes \sigma_i)\rho(I \otimes \sigma_i)^\dagger, \tag{15}$$

where the coefficients a_i and b_i are determined by the error probabilities of the two sequential channels:

$$\begin{aligned} a_0 &= p_{10}p_{20} + p_{11}p_{21} + p_{12}p_{22} + p_{13}p_{23}, \\ a_1 &= p_{10}p_{21} + p_{11}p_{20}, \\ a_2 &= p_{10}p_{22} + p_{12}p_{20}, \\ a_3 &= p_{10}p_{23} + p_{13}p_{20}, \end{aligned} \tag{16}$$

and

$$\begin{aligned} b_0 &= 0, \\ b_1 &= p_{12}p_{23} + p_{13}p_{22}, \\ b_2 &= p_{11}p_{23} + p_{13}p_{21}, \\ b_3 &= p_{11}p_{22} + p_{12}p_{21}. \end{aligned} \tag{17}$$

The coefficients a_i and b_i arise from different classes of Pauli error pairs. In a fixed causal structure, these two classes add incoherently, such as a_i+b_i in Eq. (15), yielding an effective Pauli channel. In the quantum switch scenario, however, the control measurement separates them, the a_i and b_i are routed to different conditional branches, and this separation is the origin of the QFI enhancement.

After Alice performs the standard teleportation protocol, the output state at Bob's side is

$$\begin{aligned} \rho_{\text{out}}^{\text{fo}} &= [(a_0+a_3+b_3)\alpha^2 + (a_1+a_2+b_1+b_2)|\beta|^2]\,|0\rangle\langle 0| \\ &+ [(a_1+a_2+b_1+b_2)\alpha^2 + (a_0+a_3+b_3)|\beta|^2]\,|1\rangle\langle 1| \\ &+ [(a_0-a_3-b_3)\alpha\beta^\dagger + (a_1-a_2+b_1-b_2)\alpha\beta]\,|0\rangle\langle 1| \\ &+ [(a_1-a_2+b_1-b_2)\alpha\beta^\dagger + (a_0-a_3-b_3)\alpha\beta]\,|1\rangle\langle 0|, \end{aligned} \tag{18}$$

where $\alpha = \cos\frac{\theta}{2}$ and $\beta = e^{i\phi}\sin\frac{\theta}{2}$.

Applying the Bloch-vector formalism of Eq. (4), the QFI retained under the fixed causal order is

$$\mathcal{F}^{\text{fo}} = \begin{cases} M, & \text{if } |\boldsymbol{\omega}| = 1, \\ M + \frac{(B^2-A^2)^2\sin^4\theta\sin^2 2\phi}{4(1-|\boldsymbol{\omega}|^2)}, & \text{if } |\boldsymbol{\omega}| < 1, \end{cases} \tag{19}$$

where $M = \sin^2\theta(A^2\sin^2\phi + B^2\cos^2\phi)$, $|\boldsymbol{\omega}| = \sqrt{N + C^2\cos^2\theta}$, $N = \sin^2\theta(A^2\cos^2\phi + B^2\sin^2\phi)$, $A = a_0 + a_1 - a_2 - a_3 + b_1 - b_2 - b_3$, $B = a_0 - a_1 + a_2 - a_3 - b_1 + b_2 - b_3$, and $C = a_0 - a_1 - a_2 + a_3 - b_1 - b_2 + b_3$.

This result serves as the fixed-order benchmark against which the quantum-switch-assisted protocol will be compared. In the next subsection, we replace the fixed causal sequence with a coherent superposition of channel orders, the quantum switch, and examine whether causal control can overcome the limitations of conventional noise accumulation.

B. QFI Teleportation under single quantum switch

In the quantum-switch-assisted protocol, the ordering of the two noisy channels is controlled by an auxiliary qubit, rather than being fixed in advance. Consequently, the particle transmitted to Bob simultaneously experiences two alternative causal trajectories, corresponding to $\mathcal{E}_2 \circ \mathcal{E}_1$ and $\mathcal{E}_1 \circ \mathcal{E}_2$. This higher-order control of quantum channels leads to a joint state of the target system and the control qubit, where the causal degree of freedom becomes correlated with the noisy evolution.

For two Pauli channels with Kraus operators E_{1i}^B and E_{2j}^B, the quantum-switch evolution yields the joint target-control state

$$\begin{aligned} \rho_{ABC}^{\text{qs}} &= S(\mathcal{E}_1, \mathcal{E}_2)(\rho_{AB}\otimes\rho_C) \\ &= \frac{1}{4}\sum_{ij}\Big(\Big\{E_{2j}^B, E_{1i}^B\Big\}\rho_{AB}\Big\{E_{2j}^B, E_{1i}^B\Big\}^\dagger \otimes |+\rangle_C\langle +| \\ &+ \Big\{E_{2j}^B, E_{1i}^B\Big\}\rho_{AB}\Big[E_{2j}^B, E_{1i}^B\Big]^\dagger \otimes |+\rangle_C\langle -| \\ &+ \Big[E_{2j}^B, E_{1i}^B\Big]\rho_{AB}\Big\{E_{2j}^B, E_{1i}^B\Big\}^\dagger \otimes |-\rangle_C\langle +| \\ &+ \Big[E_{2j}^B, E_{1i}^B\Big]\rho_{AB}\Big[E_{2j}^B, E_{1i}^B\Big]^\dagger \otimes |-\rangle_C\langle -|\Big), \end{aligned} \tag{20}$$

where $\{.,.\}$ and $[.,.]$ denote the anti-commutator and commutator, respectively.

Because the control qubit is correlated with the target system, extracting a usable entanglement resource requires measuring it. We measure the control qubit projectively in the basis $\{|+\rangle, |-\rangle\}$, where $|\pm\rangle = (|0\rangle \pm |1\rangle)/\sqrt{2}$. The outcome $|+\rangle$ selects the anti-commutator contribution of Eq. (20), while $|-\rangle$ selects the commutator contribution. Each outcome yields a different effective entangled state shared between Alice and Bob.

$$\begin{aligned} \rho_{AB}^{+} &= \frac{1}{4Q_+}\sum_{ij}\Big\{E_{2j}^B, E_{1i}^B\Big\}\rho_{AB}\Big\{E_{2j}^B, E_{1i}^B\Big\}^\dagger, \\ \rho_{AB}^{-} &= \frac{1}{4Q_-}\sum_{ij}\Big[E_{2j}^B, E_{1i}^B\Big]\rho_{AB}\Big[E_{2j}^B, E_{1i}^B\Big]^\dagger, \end{aligned} \tag{21}$$

where Q_+ and Q_- represent the probabilities of obtaining the outcomes $|+\rangle$ and $|-\rangle$. This two-branch decomposition separates the contributions of commuting and anti-commuting Kraus-operator pairs, providing a trajectory-level description of the Pauli-channel evolution.

The physical content of Eqs. (20) and (21) can be read directly at the level of each error pair. The two order combine as $\mathcal{A}_{ij}^{(\pm)} = E_{2j}E_{1i} \pm E_{1i}E_{2j}$. If the pair commutes, $\mathcal{A}_{ij}^{(-)} = 0$ and that trajectory is tagged by the $|+\rangle$ control outcome. If it anti-commutes, $\mathcal{A}_{ij}^{(+)} = 0$ and the trajectory is tagged by $|-\rangle$. Thus, the control measurement acts as a coherent trajectory label: it does not make either physical error less likely, but prevents the two algebraic sectors from being mixed in the same conditional state. The complete routing is summarized graphically in Fig. 2(a) for the binary $X+Y$ example and Fig. 2(b) for two independent identical channel pairs.

In this section only Bob's qubit experiences the noise, so the conditional entangled states reduce to

$$\begin{aligned} \rho_{AB}^{+} &= \frac{1}{Q_+}\sum_{i=0}^{3} a_i\,(I\otimes\sigma_i)\,\rho_{AB}\,(I\otimes\sigma_i), \\ \rho_{AB}^{-} &= \frac{1}{Q_-}\sum_{i=0}^{3} b_i\,(I\otimes\sigma_i)\,\rho_{AB}\,(I\otimes\sigma_i), \end{aligned} \tag{22}$$

Here, $Q_+ = \sum_{i=0}^{3} a_i$ and $Q_- = \sum_{i=0}^{3} b_i$. The coefficients a_i and b_i are the unnormalized trajectory weights

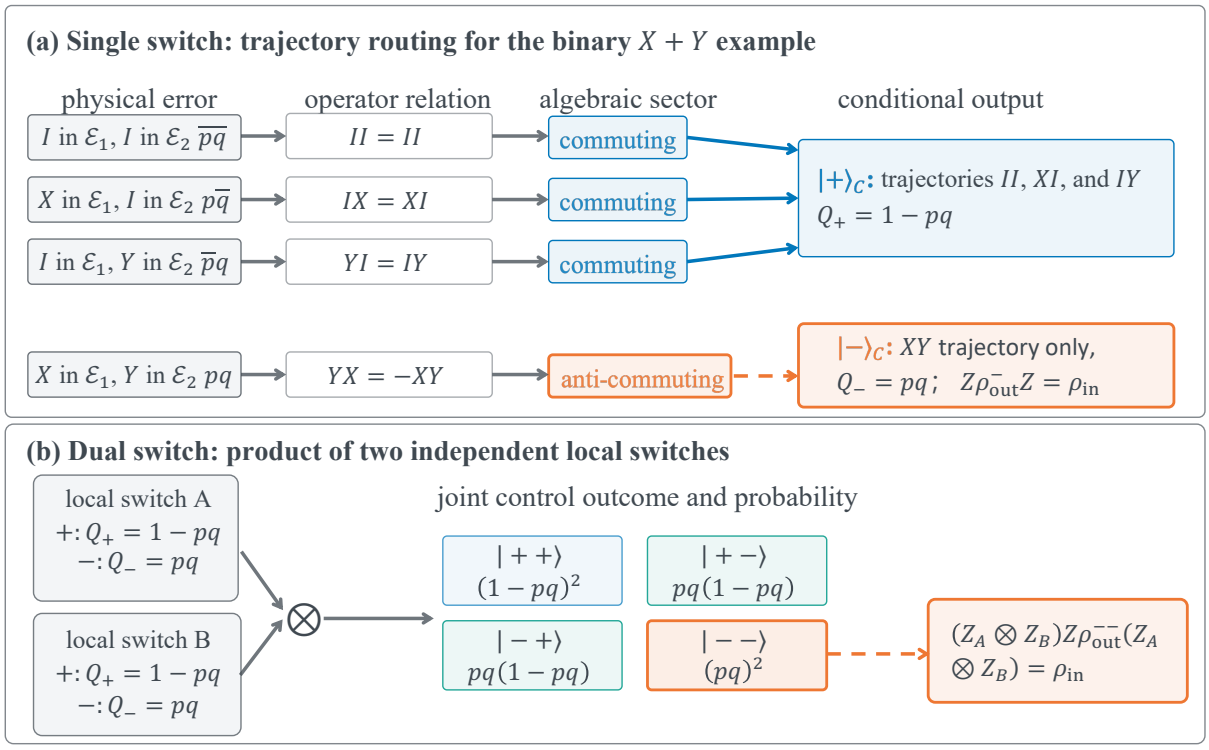


FIG. 2: Error-trajectory routing underlying quantum-switch-assisted QFI teleportation. (a) For the binary $X + Y$ example, the commuting Kraus events II, XI, and IY are routed exclusively to the $|+\rangle_C$ anti-commutator branch, with $Q_+ = 1 - pq$. For the other trajectory, the two orders give $YX = -iZ$ and $XY = iZ$; they cancel at the $|+\rangle_C$ port and add at the $|-\rangle_C$ port. Thus, $Q_- = pq$, and the minus branch contains one known Z rotation, up to a global phase. A Z operation restores the ideal state without requiring knowledge of p, q, or ϕ. The switch labels the algebraic sectors but does not alter the physical trajectory probabilities. (b) For two independent identical channel pairs, the joint outcomes are the product of the local labels. The $|--\rangle$ branch occurs with $Q_{--} = (pq)^2$ and carries $Z_A \otimes Z_B$; because $(Z_A \otimes Z_B)\rho_{\text{out}}^{--}(Z_A \otimes Z_B) = \rho_{\text{in}}$, the Bell resource and teleported state are ideal in this symmetric branch.

in the anti-commutator and commutator branches, respectively; division by $Q_\pm$ produces the conditional Pauli distributions.

After obtaining the conditional entangled resources, Alice and Bob perform the standard teleportation protocol. The two branches lead to different output states and, consequently, to different amounts of preserved QFI. For the $|+\rangle$ branch, the corresponding output state is

$$\begin{aligned}\rho_{\text{out}}^{+} = \frac{1}{Q_+}\Big\{&\left[(a_0+a_3)\,\alpha^2 + (a_1+a_2)\,|\beta|^2\right]|0\rangle\langle 0| \\ &+ \left[(a_1+a_2)\,\alpha^2 + (a_0+a_3)\,|\beta|^2\right]|1\rangle\langle 1| \\ &+ \left[(a_0-a_3)\,\alpha\beta^\dagger + (a_1-a_2)\,\alpha\beta\right]|0\rangle\langle 1| \\ &+ \left[(a_1-a_2)\,\alpha\beta^\dagger + (a_0-a_3)\,\alpha\beta\right]|1\rangle\langle 0|\Big\}.\end{aligned} \tag{23}$$

Using the Bloch-vector representation introduced previously, the corresponding QFI for the encoded phase parameter ϕ is

$$\mathcal{F}^{+} = \begin{cases} \frac{M_+}{Q_+^2}, & \text{if } |\boldsymbol{\omega}_+| = 1, \\ \frac{M_+}{Q_+^2} + \frac{(B_+^2 - A_+^2)^2 \sin^4\theta \sin^2 2\phi}{4(Q_+)^4\left(1-|\boldsymbol{\omega}_+|^2\right)}, & \text{if } |\boldsymbol{\omega}_+| < 1, \end{cases} \tag{24}$$

where $M_+ = \sin^2\theta(A_+^2\sin^2\phi + B_+^2\cos^2\phi)$, $|\boldsymbol{\omega}_+| = \frac{1}{Q_+}\sqrt{N_+ + C_+^2\cos^2\theta}$, $N_+ = \sin^2\theta(A_+^2\cos^2\phi + B_+^2\sin^2\phi)$, $A_+ = a_0+a_1-a_2-a_3$, $B_+ = a_0-a_1+a_2-a_3$, and $C_+ = a_0 - a_1 - a_2 + a_3$.

For the $|-\rangle$ branch, the output state is

$$\begin{aligned}\rho_{\text{out}}^{-} = \frac{1}{Q_-}\Big\{&\left[b_3\alpha^2 + (b_1+b_2)|\beta|^2\right]|0\rangle\langle 0| \\ &+ \left[(b_1+b_2)\alpha^2 + b_3|\beta|^2\right]|1\rangle\langle 1| \\ &+ \left[-b_3\alpha\beta^\dagger + (b_1-b_2)\alpha\beta\right]|0\rangle\langle 1| \\ &+ \left[(b_1-b_2)\alpha\beta^\dagger - b_3\alpha\beta\right]|1\rangle\langle 0|\Big\}.\end{aligned} \tag{25}$$

Then, the QFI can be obtained as

$$\mathcal{F}^{-}=\begin{cases}\frac{M_-}{Q_-^2}, & \text{if } |\boldsymbol{\omega}_-|=1,\\ \frac{M_-}{Q_-^2}+\frac{(B_-^2-A_-^2)^2\sin^4\theta\sin^2 2\phi}{4(Q_-)^4\left(1-|\boldsymbol{\omega}_-|^2\right)}, & \text{if } |\boldsymbol{\omega}_-|<1.\end{cases} \tag{26}$$

Here, $M_- = \sin^2\theta(A_-^2\sin^2\phi + B_-^2\cos^2\phi)$, $|\boldsymbol{\omega}_-| = \frac{1}{Q_-}\sqrt{N_- + C_-^2\cos^2\theta}$, $N_- = \sin^2\theta(A_-^2\cos^2\phi + B_-^2\sin^2\phi)$, $A_- = b_1 - b_2 - b_3$, $B_- = -b_1 + b_2 - b_3$, and $C_- = -b_1 - b_2 + b_3$.

Given the probabilistic nature of the two measurement outcomes, the metrological information retained by preserving the labeling of control outcomes can be quantitatively characterized by the outcome-resolved QFI

$$\mathcal{F}^{\mathrm{qs}} = Q_+\mathcal{F}^{+} + Q_-\mathcal{F}^{-}. \tag{27}$$

Equation (27) provides the theoretical basis for comparing the quantum-switch-assisted protocol with the fixed-order scheme. In the following, we apply this framework to representative composite Pauli noise configurations and demonstrate that causal superposition can modify QFI degradation and, under certain conditions, enable perfect QFI recovery in a selected conditional branch.

Because the branch probabilities $Q_\pm$ are independent of the encoded phase ϕ in the present model, Eq. (27) is also the QFI that retains the control-outcome label. If both labeled outcomes are used, no event need be discarded at this stage. If only the perfectly recoverable $|-\rangle$ branch is selected, however, the information per input trial is $Q_-\mathcal{F}^-$ rather than $\mathcal{F}^-$.

C. Single-Switch-Assisted QFI Teleportation under Typical Pauli Channels

To illustrate the performance improvement brought by the quantum switch, we now analyze three representative composite Pauli channels. For each case, we substitute the specific error probabilities into the general formalism and compare the QFI teleportation performance between the fixed-order and single-switch-assisted configurations.

1. *Bit-flip (X) and Bit-phase-flip (Y) channels*

We first consider composite noise consisting of a bit-flip (X) channel and a bit-phase-flip (Y) channel. The error probabilities are $p_{10} = 1-p, p_{11} = p, p_{20} = 1-q, p_{22} = q$, with all other probabilities being zero. For comparison, we first consider fixed-order teleportation. Substituting the above probabilities into Eq. (18), Bob's output state becomes

$$\begin{aligned}\rho_{\mathrm{out,XY}}^{\mathrm{fo}} =& \left[(\bar{p}-q+2pq)\,\alpha^2 + (p+q-2pq)\,|\beta|^2\right]|0\rangle\langle 0|\\ &+\left[(p+q-2pq)\,\alpha^2 + (\bar{p}-q+2pq)\,|\beta|^2\right]|1\rangle\langle 1|\\ &+\left[(\bar{p}-q)\,\alpha\beta^\dagger + (p-q)\,\alpha\beta\right]|0\rangle\langle 1|\\ &+\left[(p-q)\,\alpha\beta^\dagger + (\bar{p}-q)\,\alpha\beta\right]|1\rangle\langle 0|,\end{aligned} \tag{28}$$

where we use the notation $\bar{\square} = 1-\square$.

When the quantum switch is introduced, the causal relation between the two channels becomes coherently controlled. The output evolution is separated into two conditional branches according to the measurement outcome of the control qubit. For the $|+\rangle$ branch, the resulting state is

$$\begin{aligned}\rho_{\mathrm{out,XY}}^{+} =& \frac{1}{1-pq}\left\{[\bar{p}\bar{q}\alpha^2 + (p+q-2pq)|\beta|^2]\,|0\rangle\langle 0|\right.\\ &+[(p+q-2pq)\alpha^2 + \bar{p}\bar{q}|\beta|^2]\,|1\rangle\langle 1|\\ &+[\bar{p}\bar{q}\alpha\beta^\dagger + (p-q)\alpha\beta]\,|0\rangle\langle 1|\\ &\left.+[(p-q)\alpha\beta^\dagger + \bar{p}\bar{q}\alpha\beta]\,|1\rangle\langle 0|\right\}.\end{aligned} \tag{29}$$

This branch remains affected by the Pauli errors.

In contrast, the $|-\rangle$ branch exhibits a different behavior. After substituting the $X+Y$ noise parameters into the general expression, the output state becomes

$$\rho_{\mathrm{out,XY}}^{-} = \alpha^2\,|0\rangle\langle 0| + |\beta|^2\,|1\rangle\langle 1| - \alpha\beta^\dagger\,|0\rangle\langle 1| - \alpha\beta\,|1\rangle\langle 0|. \tag{30}$$

This state differs from the ideal input state only by a known unitary transformation. Therefore, after applying the corresponding ϕ-independent unitary operation, the original quantum state can be perfectly recovered: $Z\rho_{\mathrm{out,XY}}^{-}Z = |\psi\rangle_{\mathrm{in}}\langle\psi|$. This example makes the error-trajectory picture explicit. As illustrated in Fig. 2(a), the anti-commuting error has weight pq and satisfies $[X,Y] = 2iZ$, so it is routed exclusively to the $|-\rangle$ branch. Consequently, $Q_- = pq$ and the normalized branch differs from the input only by the operation Z. The factors p and q cancel from the normalized state in Eq. (30). The remaining trajectories contain at least one identity operation, populate the $|+\rangle$ branch with $Q_+ = 1-pq$, and retain a probability-dependent Pauli mixture. This explains intuitively why Eqs. (29) and (30) have very different dependence on p and q.

This result highlights a central point: the quantum switch does not reduce the physical error probabilities. Rather, it separates the anti-commutator and commutator contributions of Eq. (20) into distinct conditional branches, one of which can become correctable by a parameter-independent unitary. The advantage is a consequence of causal reorganization, not noise suppression.

We now quantify the enhancement by comparing the QFI under the fixed-order and quantum-switch protocols. The analytical expressions for $\mathcal{F}_{\mathrm{XY}}^{\mathrm{fo}}$ and $\mathcal{F}_{\mathrm{XY}}^{+}$ can be obtained from Eqs. (19) and (24), but their closed forms are too complicated to display; we therefore present the results graphically. Figure 3 compares the QFI behavior

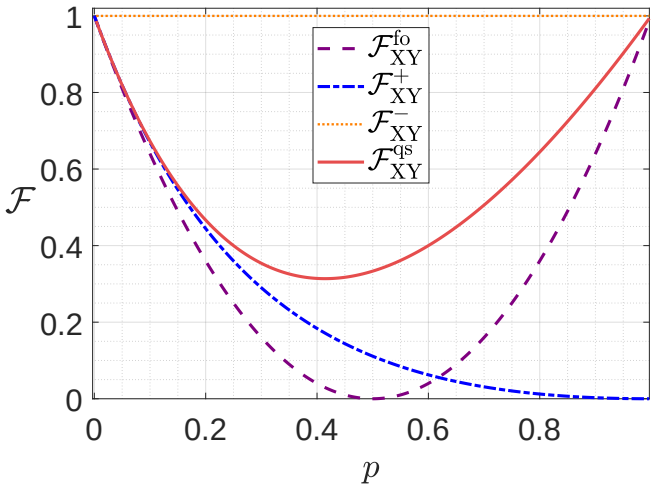


FIG. 3: Single-switch-assisted QFI of the teleported qubit under $X+Y$ noise as both error probabilities are varied synchronously from 0 to 1 along the diagonal $q=p$, with $\theta=\phi=\pi/2$.

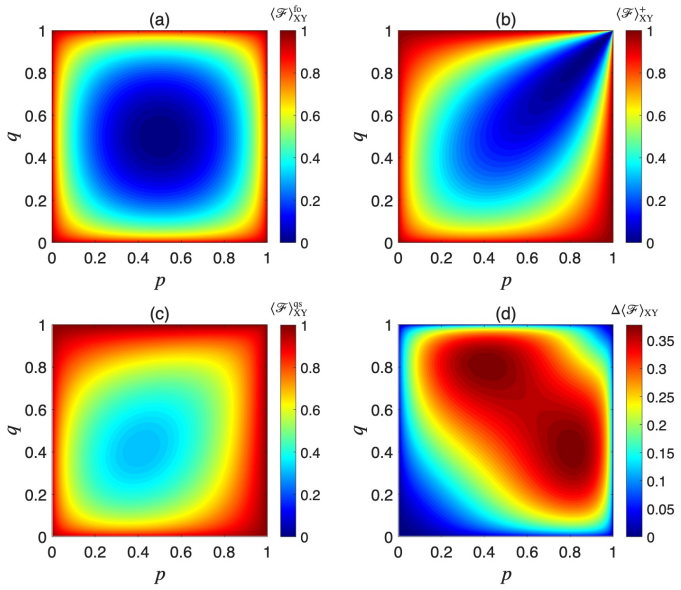


FIG. 4: Phase-averaged QFI $\langle\mathcal{F}\rangle_{\rm XY}$ as a function of the error probabilities p and q for the composite $X+Y$ channel at $\theta=\pi/2$. (a) Fixed-order QFI $\langle\mathcal{F}\rangle_{\rm XY}^{\rm fo}$; (b) conditional QFI of the $|+\rangle$ branch $\langle\mathcal{F}\rangle_{\rm XY}^{+}$; (c) the outcome-resolved QFI $\langle\mathcal{F}\rangle_{\rm XY}^{\rm qs}$; and (d) the quantum-switch enhancement $\Delta\langle\mathcal{F}\rangle_{\rm XY}=\langle\mathcal{F}\rangle_{\rm XY}^{\rm qs}-\langle\mathcal{F}\rangle_{\rm XY}^{\rm fo}$.

under fixed causal order and single-switch-assisted teleportation for the composite $X+Y$ Pauli noise. In the fixed-order scenario, the sequential action of two non-commuting Pauli channels produces an effective Pauli mixture, where different error trajectories are added incoherently. Consequently, the encoded phase information gradually decreases as the noise probability approaches the maximally stochastic point 1/2, leading to a pronounced decrease of $\mathcal{F}_{\rm XY}^{\rm fo}$ (dashed line).

In contrast, the quantum switch does not suppress either the X or Y error probability. Instead, it decomposes the evolution into branches governed by the commutator and anti-commutator of the Kraus operators. The fact that $\mathcal{F}_{\rm XY}^{-}$ remains unity whenever $Q_{-}>0$ confirms Eq. (30). The $|+\rangle$ branch retains a probability-dependent Pauli mixture. Retaining the control record makes the outcome-resolved average $\mathcal{F}_{\rm XY}^{\rm qs}$ at least as large as the QFI obtained after the record is discarded, with strict gains away from equality points. The enhancement can be further quantified by

$$\Delta\mathcal{F}=\mathcal{F}^{\rm qs}-\mathcal{F}^{\rm fo}. \tag{31}$$

The nonnegative value of $\Delta\mathcal{F}$ throughout the parameter space, with equality at special boundary points, quantifies the advantage of retaining the control label in the considered $X+Y$ model.

In practice the phase ϕ is unknown, so we also evaluate the phase-averaged QFI,

$$\langle\mathcal{F}\rangle=\frac{1}{2\pi}\int_0^{2\pi}\mathcal{F}(\phi)d\phi. \tag{32}$$

The quantity $\langle\mathcal{F}\rangle$ is an arithmetic average of local QFIs. At each value of ϕ, the local QFI assumes a locally unbiased estimation problem and permits the optimal measurement to depend on the operating point. Averaging those already optimized local quantities therefore does not define a single globally implementable measurement. In a Bayesian estimation problem, by contrast, the phase is assigned a prior distribution, and one optimizes one parameter-independent measurement and estimator for a prior-averaged cost (or its Bayesian information bound); the prior information and the global measurement constraint enter before the optimization [82]. In general, that optimization does not commute with the phase average. We use $\langle\mathcal{F}\rangle$ only as a working-point-independent diagnostic for comparing how the same channels retain local parameter sensitivity.

Figure 4 further demonstrates that the enhancement provided by the quantum switch is not restricted to a particular phase-estimation working point. By averaging the QFI over the unknown phase parameter, the dependence on a specific encoding phase is removed, allowing the intrinsic influence of causal reorganization to be revealed. For the fixed-order protocol, the phase-averaged QFI exhibits a strong degradation in the intermediate noise regime, as shown in Fig. 4(a). This originates from the fact that the composite $X+Y$ channel becomes maximally random when both error probabilities approach comparable values, resulting in severe decoherence of the encoded parameter. Notice that $p=1$ (or $q=1$) corresponds to a deterministic X (or Y) operation rather than maximal decoherence. Hence, the recovery of QFI when p and q increase beyond 1/2 should be understood as a

crossover from stochastic Pauli mixing to a deterministic unitary operation, rather than as a reversal of monotonically increasing noise. The quantum-switch-assisted protocol changes this behavior qualitatively. Although the $|+\rangle$ branch still suffers from residual decoherence, the $|-\rangle$ branch isolates the anti-commuting error trajectories. Therefore, the outcome-resolved QFI $\langle\mathcal{F}\rangle^{\rm qs}_{\rm XY}$ is no smaller than $\langle\mathcal{F}\rangle^{\rm fo}_{\rm XY}$ for this model. The positive enhancement region in Fig. 4(d) confirms that the advantage of the quantum switch is a structural consequence of causal-order superposition rather than a state-dependent optimization.

2. *Bit-flip (X) and Phase-flip (Z) channels*

We now consider composite noise consisting of a bit-flip (X) channel and a phase-flip (Z) channel. Unlike the $X+Y$ case, the two error types have qualitatively different effects: X interchanges the computational basis states, while Z directly degrades the phase coherence that carries the metrological information. The $X+Z$ combination therefore isolates the effect of causal superposition on phase-sensitive decoherence.

We set $p_{10}=1-p, p_{11}=p, p_{20}=1-q, p_{23}=q$, with all other error probabilities to be zero. Substituting these parameters into the general expressions derived above, the output state under fixed causal order is obtained as

$$\begin{aligned}\rho^{\rm fo}_{\rm out,XZ} =&[\bar{p}\alpha^2+p|\beta|^2]\,|0\rangle\langle 0|+[p\alpha^2+\bar{p}|\beta|^2]\,|1\rangle\langle 1|\\ &+[\bar{p}(1-2q)\alpha\beta^\dagger+p(1-2q)\alpha\beta]\,|0\rangle\langle 1|\\ &+[p(1-2q)\alpha\beta^\dagger+\bar{p}(1-2q)\alpha\beta]\,|1\rangle\langle 0|\,.\end{aligned}\tag{33}$$

In the fixed-order scenario, the phase coherence terms contain the factor $1-2q$ from the phase-flip channel. Their magnitude decreases as q approaches the maximally stochastic point $1/2$ and increases again as the channel approaches the deterministic Z operation at $q=1$.

Under the single-switch-assisted protocol, the two causal branches exhibit distinct behaviors. For the $|-\rangle$ measurement outcome, the output state reduces to

$$\rho^{-}_{\rm out,XZ}=|\beta|^2|0\rangle\langle 0|+\alpha^2|1\rangle\langle 1|-\alpha\beta|0\rangle\langle 1|-\alpha\beta^\dagger|1\rangle\langle 0|.\tag{34}$$

This state can be transformed into the original input state through an appropriate unitary operation, yielding $\mathcal{F}^{-}_{\rm XZ}=\sin^2\theta$. Therefore, the perfect-transmission branch observed in the $X+Y$ case also appears for this binary $X+Z$ pair, for which $[X,Z]=-2iY$.

For the $|+\rangle$ branch, however, the output state remains affected by the residual phase noise,

$$\begin{aligned}\rho^{+}_{\rm out,XZ} =&\frac{1}{1-pq}\big\{[\bar{p}\alpha^2+p\bar{q}|\beta|^2]\,|0\rangle\langle 0|\\ &+[p\bar{q}\alpha^2+\bar{p}|\beta|^2]\,|1\rangle\langle 1|\\ &+[\bar{p}(1-2q)\alpha\beta^\dagger+p\bar{q}\alpha\beta]\,|0\rangle\langle 1|\\ &+[p\bar{q}\alpha\beta^\dagger+\bar{p}(1-2q)\alpha\beta]\,|1\rangle\langle 0|\big\}\,.\end{aligned}\tag{35}$$

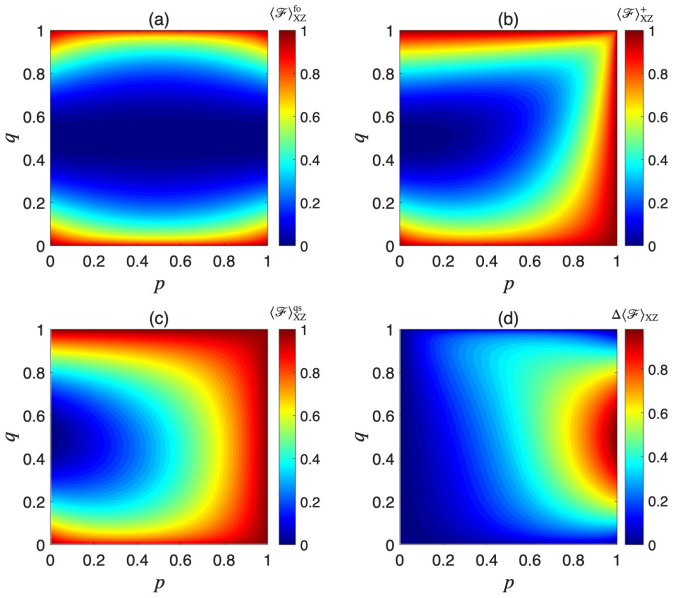


FIG. 5: Phase-averaged QFI $\langle\mathcal{F}\rangle_{\rm XZ}$ as a function of the error probabilities p and q for the composite $X+Z$ channel at $\theta=\pi/2$. (a) Fixed-order QFI $\langle\mathcal{F}\rangle^{\rm fo}_{\rm XZ}$; (b) conditional QFI of the $|+\rangle$ branch $\langle\mathcal{F}\rangle^{+}_{\rm XZ}$; (c) the outcome-resolved QFI $\langle\mathcal{F}\rangle^{\rm qs}_{\rm XZ}$; and (d) the quantum-switch enhancement $\Delta\langle\mathcal{F}\rangle_{\rm XZ}=\langle\mathcal{F}\rangle^{\rm qs}_{\rm XZ}-\langle\mathcal{F}\rangle^{\rm fo}_{\rm XZ}$.

Although the two conditional states clearly demonstrate the commutation-based separation of Pauli error trajectories, a comparison at a single phase-estimation working point does not fully reveal the difference between the $X+Y$ and $X+Z$ composite channels. In particular, the single-switch-assisted QFIs of these two noise models coincide at $\theta=\phi=\pi/2$.

To understand this apparent equivalence, we consider the equatorial input state with $\theta=\pi/2$. Under fixed causal order, the Bloch vectors corresponding to the $X+Y$ and $X+Z$ channels can be written as

$$\boldsymbol{\omega}^{\rm fo}_{\rm XY}(\phi)=\begin{pmatrix}(1-2q)\cos\phi\\(1-2p)\sin\phi\\0\end{pmatrix},\tag{36}$$

and

$$\boldsymbol{\omega}^{\rm fo}_{\rm XZ}(\phi)=\begin{pmatrix}(1-2q)\cos\phi\\(1-2p)(1-2q)\sin\phi\\0\end{pmatrix},\tag{37}$$

respectively. At $\phi=\pi/2$, the tangent vector $\partial_\phi\boldsymbol{\omega}$ is directed entirely along the x axis. Since the two channels possess the same x-direction contraction factor, namely $1-2q$, they yield the same local QFI at this working point. A similar relation holds for the $|+\rangle$ branch, while their $|-\rangle$ branches both preserve the ideal QFI. Consequently, the equality observed along $p=q$ is therefore a

particular slice of a more general working-point, rather than evidence that the two composite channels are physically equivalent. To avoid drawing conclusions from this special phase point, we first average the local QFI over the full phase interval. The phase average QFI $\langle\mathcal{F}\rangle$ samples both equatorial directions and therefore reveals the different anisotropic contractions generated by the $X+Y$ and $X+Z$ channels.

Figure 5 illustrates the resulting phase average QFI landscapes. Figure 5(a) shows a pronounced horizontal valley around $q=1/2$. At this point, the phase-flip channel is maximally stochastic between I and Z. The output state is maximally mixed for the equatorial input, yielding $\langle\mathcal{F}\rangle^{\rm fo}_{\rm XZ}=0$, independently of p. Figure 5(b) shows that the $|+\rangle$-branch QFI is generally nonmonotonic. This behavior results from the conditional removal of the XZ trajectory and the subsequent renormalization of the remaining commuting sector. In particular, for $p=1$ the $|+\rangle$ branch contains only the deterministic X operation, whereas for $q=1$ it contains only the deterministic Z operation. The large conditional QFI near these boundaries therefore reflects an increasingly deterministic conditional channel. Taking both control outcomes into account, the outcome-resolved QFI of the single-switch protocol is presented in Fig. 5(c). The enhancement therefore becomes particularly pronounced when the contribution of perfectly preserved $|-\rangle$-sector is counted. The enhancement in Fig. 5(d) is a direct manifestation of causal error-trajectory factorization. It is not difficult to understand that the largest enhancement occurs around $p=1$ and $q=1/2$. At this point, the fixed-order channel produces an unflagged equal mixture of the X and XZ trajectories, which completely erases the phase information. The quantum switch, in contrast, routes the X and XZ trajectories to different control outcomes.

Although the phase-averaged QFI provides a working-point-independent characterization of the overall metrological performance, the averaging procedure removes the directional response of the $X+Z$ channel on the equatorial Bloch plane. It therefore does not reveal whether the enhancement is distributed uniformly over ϕ or concentrated around particular phase-estimation working points. The difference becomes apparent when $\theta=\pi/2$ and $\phi=\pi$. The fixed-order QFIs are $\mathcal{F}^{\rm fo}_{\rm XY}(\pi)=(1-2p)^2$ and $\mathcal{F}^{\rm fo}_{\rm XZ}(\pi)=(1-2p)^2(1-2q)^2$. This clearly indicates that $X+Z$ has an additional attenuation factor induced by the phase-flip channel. The distinction persists in the $|+\rangle$ branch because $\mathcal{F}^{+}_{\rm XY}(\pi)=\left(\frac{1-2p+pq}{1-pq}\right)^2$, whereas $\mathcal{F}^{+}_{\rm XZ}(\pi)=\left(\frac{1-2p-2q+3pq}{1-pq}\right)^2$.

A quantitative explanation follows along the diagonal $p=q=r$ used in Fig. 6. For $\theta=\pi/2$, $\phi=\pi$, and $0\le r<1$, Eq. (35) gives

$$\mathcal{F}^{+}_{\rm XZ}(r)=\left(\frac{1-3r}{1+r}\right)^2,\qquad \frac{d\mathcal{F}^{+}_{\rm XZ}}{dr}=\frac{8(3r-1)}{(1+r)^3}. \tag{38}$$

Thus, the $|+\rangle$-branch QFI decreases to zero at $r=1/3$ and increases for $r>1/3$. This turnover does not result from an increasing commutator weight: the $|+\rangle$ outcome contains the commuting trajectories II, XI, and IZ, with total probability $Q_+=1-r^2$, whereas the anti-commuting XZ trajectory is in the $|-\rangle$ branch with $Q_-=r^2$. Within the normalized $|+\rangle$ state, the three surviving trajectories act with opposite signs on the direction of the equatorial Bloch vector. Their signed factor is $(1-3r)/(1+r)$; it cancels at $r=1/3$ and regains magnitude as the conditional channel approaches a more deterministic Pauli operation. The rise at large r therefore reflects conditional normalization and a crossover from stochastic mixing toward a deterministic unitary, not a monotonic reduction of physical noise. When r approaches 1, the growing probability $Q_-=r^2$ of the perfectly correctable branch separately contributes to the outcome-resolved average in Eq. (27).

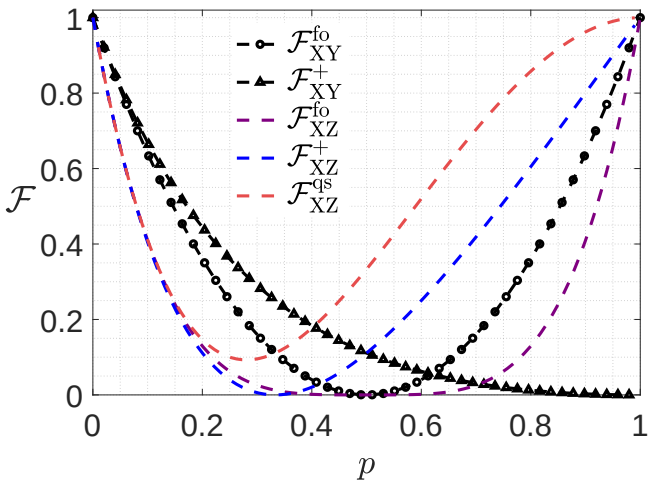


FIG. 6: Single-switch-assisted QFI of the teleported qubit under $X+Z$ noise as both error probabilities are varied synchronously from 0 to 1 along the diagonal $q=p$. Results for $\mathcal{F}^{\rm fo}_{\rm XY}$ and $\mathcal{F}^{+}_{\rm XY}$ are plotted for comparison. The other parameters are $\theta=\pi/2$ and $\phi=\pi$.

3. *Bit-phase-flip (Y) and Phase-flip (Z) channels*

To complete the set of anti-commuting Pauli pairs, we consider the remaining combination: a bit-phase-flip (Y) channel followed by a phase-flip (Z) channel. The corresponding probabilities are chosen as $p_{10}=1-p, p_{12}=p, p_{20}=1-q, p_{23}=q$, with all other probabilities being zero.

Unlike the $X+Y$ and $X+Z$ cases, this combination replaces X with Y. Since X and Y are related by a unitary rotation around the Z axis, the causal-reorganization mechanism is expected to remain unchanged, with only the ϕ-dependence of the resulting QFI modified.

Substituting these parameters into the general expres-

sions derived previously, the fixed-order output state is obtained as

$$\begin{aligned}\rho^{\mathrm{fo}}_{\mathrm{out,YZ}} =&[\bar{p}\alpha^2 + p|\beta|^2]\,|0\rangle\langle 0| \\ &+[p\alpha^2 + \bar{p}|\beta|^2]\,|1\rangle\langle 1| \\ &+[\bar{p}(1-2q)\alpha\beta^\dagger - p(1-2q)\alpha\beta]\,|0\rangle\langle 1| \\ &+[-p(1-2q)\alpha\beta^\dagger + \bar{p}(1-2q)\alpha\beta]\,|1\rangle\langle 0|\,.\end{aligned} \tag{39}$$

As in the previous noise models, the quantum switch separates the evolution into two conditional branches. For the $|-\rangle$ branch, the output state becomes

$$\rho^{-}_{\mathrm{out,YZ}} = |\beta|^2|0\rangle\langle 0| + \alpha^2|1\rangle\langle 1| + \alpha\beta|0\rangle\langle 1| + \alpha\beta^\dagger|1\rangle\langle 0|. \tag{40}$$

After a suitable unitary operation, this state is equivalent to the original input state, yielding $\mathcal{F}^{-}_{\mathrm{YZ}} = \sin^2\theta$.

For each of the three binary Pauli pairs considered in this work, the perfect conditional-QFI recovery follows from Pauli anti-commutation. The three possible pairs of distinct Pauli axes satisfy

$$[X,Y] = 2iZ, \quad [X,Z] = -2iY, \quad [Y,Z] = 2iX, \tag{41}$$

showing that the commutator generates the third Pauli operator, up to its order-dependent sign and the factor i. Consequently, each of these three *binary* noise configurations exhibits the same causal reorganization mechanism: its sole non-commuting trajectory is routed to the conditional $|-\rangle$ branch as a single correctable Pauli rotation.

The $|+\rangle$ branch remains affected by residual noise and is given by

$$\begin{aligned}\rho^{+}_{\mathrm{out,YZ}} =&\frac{1}{1-pq}\left\{[\bar{p}\alpha^2 + p\bar{q}|\beta|^2]\,|0\rangle\langle 0|\right. \\ &+ [p\bar{q}\alpha^2 + \bar{p}|\beta|^2]\,|1\rangle\langle 1| \\ &+ [\bar{p}(1-2q)\alpha\beta^\dagger - p\bar{q}\alpha\beta]\,|0\rangle\langle 1| \\ &\left.+[-p\bar{q}\alpha\beta^\dagger + \bar{p}(1-2q)\alpha\beta]\,|1\rangle\langle 0|\right\}.\end{aligned} \tag{42}$$

We emphasize that the phase-averaged QFI in the $Y+Z$ model is exactly equal to that in the $X+Z$ model shown in Fig. 5, because replacing X by Y corresponds to a unitary basis transformation, which changes only the representation of the recovered rotation but not the underlying error-factorization principle. Therefore, the QFI enhancement observed in the $Y+Z$ model provides an additional confirmation, within the three binary models studied here, that the advantage originates from Pauli algebra rather than from one specific Pauli pair.

IV. DUAL QUANTUM SWITCHES FOR DISTRIBUTED QFI TELEPORTATION

The single-switch results of Sec. III show that, for the binary composite Pauli channels considered here, the control outcome separates branch-dependent Pauli sectors. In the $|-\rangle$ branch, this separation enables perfect QFI recovery after a conditional unitary operation. In a distributed network, the entangled pair may instead be supplied by a third party, Charlie, so that both photons pass through noisy transmission arms. We first treat independent local channels, for which the joint map factorizes and one local switch is assigned to each arm. The dual-switch configuration is then a tensor-product extension of the single-switch causal control [47].

A. Distributed QFI Teleportation without Quantum Switches

We now assume that particles A and B experience the channel sequences $\mathcal{E}_1 \to \mathcal{E}_2$ and $\mathcal{E}_3 \to \mathcal{E}_4$, respectively. To distinguish this scenario from the single-arm case of Sec. III, we use the superscript or subscript "D" to indicate that noise acts on both distribution arms. The entangled state after transmission through the four noisy channels is

$$\rho^{\mathrm{fo,D}}_{AB} = \sum_{i,j,m,n=0}^{3} \left(E^A_{2j}\otimes E^B_{4n}\right)\left(E^A_{1i}\otimes E^B_{3m}\right)\rho\left(E^A_{1i}\otimes E^B_{3m}\right)^\dagger\left(E^A_{2j}\otimes E^B_{4n}\right)^\dagger, \tag{43}$$

where the Kraus operators for all four channels are

$$E_{mk} = \sqrt{p_{mk}}\sigma_k \quad m = 1,2,3,4, k = 0,1,2,3, \tag{44}$$

with $\sum_k p_{mk} = 1$ for each m, ensuring that each channel is completely positive and trace-preserving.

Substituting Eq. (44) into Eq. (43) and simplifying yields

$$\rho^{\mathrm{fo,D}}_{\mathrm{out}} = \sum_{i,j=0}^{3}(a_i+b_i)(c_j+d_j)(\sigma_i\otimes\sigma_j)\rho(\sigma_i\otimes\sigma_j)^\dagger, \tag{45}$$

where $c_0 = p_{30}p_{40} + p_{31}p_{41} + p_{32}p_{42} + p_{33}p_{43}$, $c_1 = p_{30}p_{41}+p_{31}p_{40}$, $c_2 = p_{30}p_{42}+p_{32}p_{40}$, $c_3 = p_{30}p_{43}+p_{33}p_{40}$, $d_0 = 0$, $d_1 = p_{32}p_{43} + p_{33}p_{42}$, $d_2 = p_{31}p_{43} + p_{33}p_{41}$, and $d_3 = p_{31}p_{42} + p_{32}p_{41}$. The coefficients $a_i + b_i$ and $c_j + d_j$ characterize the effective Pauli-error distributions on Alice's and Bob's arms, respectively. Their product $(a_i+b_i)(c_j+d_j)$ is the explicit independence assumption used in the analysis below.

After Alice performs the standard teleportation protocol, the output state at Bob's side is

$$
\begin{aligned}
\rho_{\text{out}}^{\text{fo,D}} =& \big\{[(a_0+a_3+b_3)(c_0+c_3+d_3)+(a_1+a_2+b_1+b_2)(c_1+c_2+d_1+d_2)]\alpha^2 \\
&+[(a_0+a_3+b_3)(c_1+c_2+d_1+d_2)+(a_1+a_2+b_1+b_2)(c_0+c_3+d_3)]|\beta|^2\big\}\,|0\rangle\langle 0| \\
&+\big\{[(a_0+a_3+b_3)(c_1+c_2+d_1+d_2)+(a_1+a_2+b_1+b_2)(c_0+c_3+d_3)]\alpha^2 \\
&+[(a_0+a_3+b_3)(c_0+c_3+d_3)+(a_1+a_2+b_1+b_2)(c_1+c_2+d_1+d_2)]|\beta|^2\big\}\,|1\rangle\langle 1| \\
&+\big\{[(a_0-a_3-b_3)(c_0-c_3-d_3)+(a_1-a_2+b_1-b_2)(c_1-c_2+d_1-d_2)]\alpha\beta^\dagger \\
&+[(a_0-a_3-b_3)(c_1-c_2+d_1-d_2)+(a_1-a_2+b_1-b_2)(c_0-c_3-d_3)]\alpha\beta\big\}\,|0\rangle\langle 1| \\
&+\big\{[(a_0-a_3-b_3)(c_1-c_2+d_1-d_2)+(a_1-a_2+b_1-b_2)(c_0-c_3-d_3)]\alpha\beta^\dagger \\
&+[(a_0-a_3-b_3)(c_0-c_3-d_3)+(a_1-a_2+b_1-b_2)(c_1-c_2+d_1-d_2)]\alpha\beta\big\}\,|1\rangle\langle 0|\,.
\end{aligned}
\tag{46}
$$

Applying the Bloch-vector formalism yields the QFI of the output state

$$
\mathcal{F}^{\text{fo,D}} = \begin{cases} M_D, & \text{if } |\boldsymbol{\omega}_D| = 1, \\ M_D + \frac{(B_D^2 - A_D^2)^2 \sin^4\theta \sin^2 2\phi}{4\left(1-|\boldsymbol{\omega}_D|^2\right)}, & \text{if } |\boldsymbol{\omega}_D| < 1, \end{cases}
\tag{47}
$$

where $M_D = \sin^2\theta(A_D^2\sin^2\phi + B_D^2\cos^2\phi)$, $|\boldsymbol{\omega}_D| = \sqrt{N_D + C_D^2\cos^2\theta}$, $N_D = \sin^2\theta(A_D^2\cos^2\phi + B_D^2\sin^2\phi)$, $A_D = (a_0+a_1-a_2-a_3+b_1-b_2-b_3)(c_0+c_1-c_2-c_3+d_1-d_2-d_3)$, $B_D = (a_0-a_1+a_2-a_3-b_1+b_2-b_3)(c_0-c_1+c_2-c_3-d_1+d_2-d_3)$, and $C_D = (a_0-a_1-a_2+a_3-b_1-b_2+b_3)(c_0-c_1-c_2+c_3-d_1-d_2+d_3)$.

B. QFI Teleportation Enhanced by a Dual Quantum Switch Configuration

Unlike a single quantum switch that coherently controls the order of operations on a single system, the dual quantum switch can simultaneously manipulate the causal order of two independent arms. The overall evolution under the dual switch is described by a supermap $S(\mathcal{E}_1,\mathcal{E}_2,\mathcal{E}_3,\mathcal{E}_4)$, which acts on the entangled state ρ_{AB} along with a two-qubit control state $\rho_{C_1C_2}$ that determines the causal order. Specifically, the two control qubits are each prepared in the $|+\rangle$ state, so that $\rho_{C_1C_2} = |++\rangle\langle++|$. The dual-switch evolution yields the joint state

$$
\begin{aligned}
&S(\mathcal{E}_1,\mathcal{E}_2,\mathcal{E}_3,\mathcal{E}_4)(\rho_{AB}\otimes\rho_{C_1C_2}) \\
&= \sum_{i,j,m,n} \mathcal{W}_{ijmn}(\rho_{AB}\otimes\rho_{C_1C_2})\mathcal{W}_{ijmn}^\dagger,
\end{aligned}
\tag{48}
$$

where $\mathcal{W}_{ijmn}$ is a four-index Kraus operator acting jointly on the two targets and two controls; it is the tensor product of the two local switch Kraus operators of Eq. (7). For the two independent local switches, its explicit form is

$$
\begin{aligned}
\mathcal{W}_{ijmn} =& (E_{2j}^A E_{1i}^A \otimes E_{4n}^B E_{3m}^B)\otimes|00\rangle_{C_1C_2}\langle 00| + (E_{2j}^A E_{1i}^A \otimes E_{3m}^B E_{4n}^B)\otimes|01\rangle_{C_1C_2}\langle 01| \\
&+(E_{1i}^A E_{2j}^A \otimes E_{4n}^B E_{3m}^B)\otimes|10\rangle_{C_1C_2}\langle 10| + (E_{1i}^A E_{2j}^A \otimes E_{3m}^B E_{4n}^B)\otimes|11\rangle_{C_1C_2}\langle 11|\,.
\end{aligned}
\tag{49}
$$

The dual-switch maps the initial superposition control state $|++\rangle$ onto four conditional branches, corresponding to the four outcomes of measuring the two control qubits in the $\{|++\rangle, |+-\rangle, |-+\rangle, |--\rangle\}$ basis. After measuring the two control qubits, the four conditional entangled states are

$$
\begin{aligned}
\rho_{AB}^{++} &= \frac{1}{Q_{++}}\sum_{i,j=0}^{3} a_i c_j\,(\sigma_i\otimes\sigma_j)\,\rho_{AB}\,(\sigma_i\otimes\sigma_j)^\dagger\,, \\
\rho_{AB}^{+-} &= \frac{1}{Q_{+-}}\sum_{i,j=0}^{3} a_i d_j\,(\sigma_i\otimes\sigma_j)\,\rho_{AB}\,(\sigma_i\otimes\sigma_j)^\dagger\,, \\
\rho_{AB}^{-+} &= \frac{1}{Q_{-+}}\sum_{i,j=0}^{3} b_i c_j\,(\sigma_i\otimes\sigma_j)\,\rho_{AB}\,(\sigma_i\otimes\sigma_j)^\dagger\,, \\
\rho_{AB}^{--} &= \frac{1}{Q_{--}}\sum_{i,j=0}^{3} b_i d_j\,(\sigma_i\otimes\sigma_j)\,\rho_{AB}\,(\sigma_i\otimes\sigma_j)^\dagger\,.
\end{aligned}
\tag{50}
$$

The normalization factors $Q_{++} = \sum_{i,j=0}^{3} a_i c_j$, $Q_{+-} = \sum_{i,j=0}^{3} a_i d_j$, $Q_{-+} = \sum_{i,j=0}^{3} b_i c_j$, and $Q_{--} = \sum_{i,j=0}^{3} b_i d_j$ are the probabilities of the four control outcomes $|{+}{+}\rangle$, $|{+}{-}\rangle$, $|{-}{+}\rangle$, and $|{-}{-}\rangle$, respectively. The explicit forms of the corresponding output states and QFIs are given in Appendix A.

The outcome-resolved QFI over the four branches is then

$$\mathcal{F}^{\mathrm{qs,D}} = \sum_{\mu,\nu} Q_{\mu\nu}\mathcal{F}^{\mu\nu}, \quad \mu,\nu \in \{+,-\}. \tag{51}$$

Because $Q_{\mu\nu}$ is independent of ϕ, Eq. (51) is exactly the QFI of the state $\sum_{\mu,\nu} Q_{\mu\nu}|\mu\nu\rangle\langle\mu\nu| \otimes \rho_{\mathrm{out}}^{\mu\nu}$ when the two-bit control record is retained and all four tagged branches are processed. Selecting only one branch instead gives the information contribution $Q_{\mu\nu}\mathcal{F}^{\mu\nu}$ per input trial, before source, transmission, Bell-measurement, and detection losses are included.

C. Example: Identical Pauli $X+Y$ Noise for Alice and Bob

As a concrete example, we consider identical $X+Y$ composite noise on both arms, i.e., $\mathcal{E}_1 = \mathcal{E}_3$ and $\mathcal{E}_2 = \mathcal{E}_4$. In this case, the coefficients are $p_{10} = p_{30} = 1-p$, $p_{11} = p_{31} = p$, $p_{20} = p_{40} = 1-q$, and $p_{22} = p_{42} = q$, with all other p_{mk} equal to zero.

In the absence of quantum switches, the fixed-order output state is

$$\begin{aligned}
\rho_{\mathrm{out}}^{\mathrm{fo,D}} = &\left(\left\{[(\bar{p}-q+2pq)^2 + (p+q-2pq)^2]\alpha^2 + [2(\bar{p}-q+2pq)(p+q-2pq)]|\beta|^2\right\}|0\rangle\langle 0|\right.\\
&+\left\{[2(\bar{p}-q+2pq)(p+q-2pq)]\alpha^2 + [(\bar{p}-q+2pq)^2 + (p+q-2pq)^2]|\beta|^2\right\}|1\rangle\langle 1|\\
&+\left\{[(\bar{p}-q)^2 + (p-q)^2]\alpha\beta^\dagger + [2(\bar{p}-q)(p-q)]\alpha\beta\right\}|0\rangle\langle 1|\\
&+\left\{[2(\bar{p}-q)(p-q)]\alpha\beta^\dagger + [(\bar{p}-q)^2 + (p-q)^2]\alpha\beta\right\}|1\rangle\langle 0|\Big).
\end{aligned} \tag{52}$$

When the quantum switches are involved, we can derive the specific forms of $\rho_{\mathrm{out}}^{\mu\nu}$, as shown in the following equation.

$$\begin{aligned}
\rho_{\mathrm{out}}^{++} =&\frac{1}{(1-pq)^2}\left(\left\{[\bar{p}^2\bar{q}^2 + (p+q-2pq)^2]\alpha^2 + [2\bar{p}\bar{q}(p+q-2pq)]|\beta|^2\right\}|0\rangle\langle 0|\right.\\
&+\left\{[2\bar{p}\bar{q}(p+q-2pq)]\alpha^2 + [\bar{p}^2\bar{q}^2 + (p+q-2pq)^2]|\beta|^2\right\}|1\rangle\langle 1|\\
&+\left\{[\bar{p}^2\bar{q}^2 + (p-q)^2]\alpha\beta^\dagger + [2\bar{p}\bar{q}(p-q)]\alpha\beta\right\}|0\rangle\langle 1| + \left\{[2\bar{p}\bar{q}(p-q)]\alpha\beta^\dagger + [\bar{p}^2\bar{q}^2 + (p-q)^2]\alpha\beta\right\}|1\rangle\langle 0|\Big),\\
\rho_{\mathrm{out}}^{+-} =&\rho_{\mathrm{out}}^{-+} = \frac{1}{pq(1-pq)}\left(\left\{pq\bar{p}\bar{q}\alpha^2 + pq(p+q-2pq)|\beta|^2\right\}|0\rangle\langle 0|\right.\\
&+\left\{pq(p+q-2pq)\alpha^2 + pq\bar{p}\bar{q}|\beta|^2\right\}|1\rangle\langle 1|\\
&+\left\{-pq\bar{p}\bar{q}\alpha\beta^\dagger - pq(p-q)\alpha\beta\right\}|0\rangle\langle 1| + \left\{-pq(p-q)\alpha\beta^\dagger - pq\bar{p}\bar{q}\alpha\beta\right\}|1\rangle\langle 0|\Big),\\
\rho_{\mathrm{out}}^{--} =&\alpha^2|0\rangle\langle 0| + |\beta|^2|1\rangle\langle 1| + \alpha\beta^\dagger|0\rangle\langle 1| + \alpha\beta|1\rangle\langle 0|,
\end{aligned} \tag{53}$$

where $Q_{++} = (1-pq)^2$, $Q_{+-} = Q_{-+} = pq(1-pq)$, and $Q_{--} = (pq)^2$. Moreover, the two local commutator operations are Z_A and Z_B, and $(Z_A \otimes Z_B)|\Phi^+\rangle = |\Phi^+\rangle$, which explains why ρ_{out}^{--} equals the ideal input directly in this symmetric case.

Figure 7 extends the trajectory-separation mechanism to the explicitly assumed case in which both photons experience independent binary $X+Y$ channel pairs. As summarized in Fig. 2(b), the four control outcomes are the Cartesian product of the local commuting and anticommuting labels. In the $|--\rangle$ branch, each arm contains the single commutator $[X,Y]$ and hence a known local Pauli rotation. Because QFI is invariant under parameter-independent unitaries, the branch already has the ideal QFI; the inverse rotations restore the ideal state and standard measurement basis. For identical arms, $Q_- = pq$ on each arm and therefore $Q_{--} = (pq)^2$; the normalized branch has unit QFI, but its contribution per launched pair is Q_{--} before Bell-measurement inefficiency and optical loss.

The comparison between $\mathcal{F}^{\mathrm{qs,D}}$ and $\mathcal{F}^{\mathrm{fo,D}}$ therefore establishes a tensor-product extension for independent,

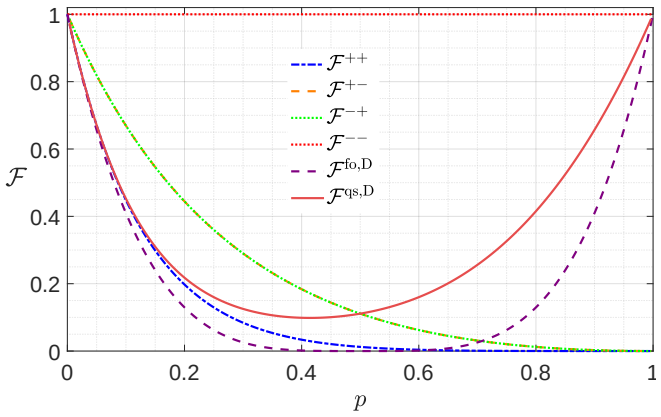


FIG. 7: Dual-switch-assisted QFI of the teleported qubit under $X+Y$ noise as both error probabilities are varied synchronously from 0 to 1 along $q=p$. The other parameters are $\theta=\phi=\pi/2$.

locally addressable channel sequences. It does not establish that two switches are universally necessary. The factorization in Eq. (43) assumes a joint Kraus structure $K_{im}=E_{1i}^{A}\otimes E_{3m}^{B}$ and product trajectory weights. A correlated Pauli channel instead has a general joint distribution $P_{\mu\nu}$ in $\mathcal{E}_{\mathrm{corr}}(\rho)=\sum_{\mu,\nu}P_{\mu\nu}(\sigma_\mu\otimes\sigma_\nu)\rho(\sigma_\mu\otimes\sigma_\nu)$, and common-mode fluctuations can also generate collective rotations or decoherence-free sectors. In such cases, a single control degree of freedom that coherently orders two correlated global maps depends on the physical dilation and correlation structure. The error-trajectories under correlated noise may not be strictly distinguishable. Thus, the dual-switch architecture is the natural per-arm construction for the independent-noise model analyzed here, whereas correlated noise requires a separate joint-channel analysis.

V. PHYSICAL INTERPRETATION OF QUANTUM-SWITCH-ASSISTED QFI TELEPORTATION

The conditional trajectory separation demonstrated in Secs. III and IV does not reduce the physical error probabilities. It follows from the coherent addition or subtraction of the two order amplitudes in Eq. (21). For the Pauli Kraus operators $E_{1i}=\sqrt{p_{1i}}\sigma_i$ and $E_{2j}=\sqrt{p_{2j}}\sigma_j$, the two sectors have a particularly transparent algebraic interpretation.

(i) **Commuting Pauli trajectories**. If E_{1i} and E_{2j} commute, as for identical Pauli matrices or an identity–Pauli pair, then $[E_{1i},E_{2j}]=0$ and $\{E_{1i},E_{2j}\}=2E_{1i}E_{2j}$. That trajectory therefore appears only in the $|+\rangle$ branch. Several such trajectories can produce different effective Pauli operations, so their unresolved mixture generally retains decoherence.

(ii) **Anti-commuting Pauli trajectories**. For two distinct nonidentity Pauli matrices, $\{E_{1i},E_{2j}\}=0$ and

$$[E_{1i},E_{2j}]=2E_{1i}E_{2j}=2i\sqrt{p_{1i}p_{2j}}\sum_k\epsilon_{ijk}\sigma_k, \qquad (54)$$

where ϵ_{ijk} is the Levi–Civita sign. The two equalities are identical: the factor of i and the ordering-dependent sign are already contained in the product $E_{1i}E_{2j}$ through $\sigma_i\sigma_j=i\sum_k\epsilon_{ijk}\sigma_k$. Reversing the order flips this sign, so the trajectory appears only in the $|-\rangle$ branch.

The control result identifies the commuting versus anti-commuting sector; it does not, in general, identify every Kraus trajectory inside that sector. Exact unitary recovery is therefore not guaranteed for an arbitrary multi-component Pauli channel. It holds for each of the three binary pairs studied here because the nonzero $|-\rangle$ sector contains only one simultaneous-error trajectory: $XY\propto Z$, $XZ\propto Y$, or $YZ\propto X$. Conditioned on the $|-\rangle$ herald, that known rotation can be inverted without knowledge of ϕ, and the normalized state has the ideal QFI.

This mechanism also distinguishes the present protocol from WMMR [36, 37]. WMMR employs a tunable weak pre-measurement followed by a reversing measurement to probabilistically filter damaging trajectories and has been developed mainly for amplitude-damping noise in the cited QFI-teleportation studies. By contrast, the quantum switch does not require weak measurement operation: stable interference between the two channel orders separates the output into two algebraic error sectors, which are identified by the control measurement. Both protocols are conditional. In the present scheme, once the desired herald is obtained, for example $|-\rangle$ or $|--\rangle$, the residual Pauli error is known and its inverse can be applied deterministically by feed-forward; however, the heralding event itself is probabilistic, with a probability that depends on p and q. Thus, the advantage demonstrated here is conditional recoverability for the three binary Pauli models considered.

More broadly, the quantum switch is complementary to established protection methods rather than a universally superior replacement. Dynamical decoupling modifies the system–environment evolution through fast, calibrated pulse sequences and can operate without post-selection when the control bandwidth is sufficient. It is particularly effective for slowly varying or spectrally structured noise, but is limited by environmental time scales and pulse imperfections [22, 28, 29]. Quantum error correction can protect a logical subspace against a broader designed error set, at the cost of redundant physical qubits or modes, ancillas, syndrome extraction, and recovery gates [26, 31, 32]. WMMR, as described above, trades conditional output quality against success probability. The dedicated comparison is summarized in Table I.

TABLE I: Comparison of quantum-noise protection strategies.

Method	Mechanism	Main resources	Recovery and rate characteristics
Dynamical decoupling	Pulse-based averaging of system-environment coupling	Fast calibrated pulses and direct system access	Usually unconditional; mainly suited to slow or structured noise; no intrinsic postselection penalty
Quantum error correction	Redundant encoding, syndrome extraction, and recovery	Multiple qubits/modes, ancillas, gates, and measurements	Broad designed-noise applicability; unconditional logical recovery in the fault-tolerant regime
WMMR	Weak pre-measurement and measurement reversal	Tunable measurements and reversal operation	Conditional enhancement with a fidelity-success-probability trade-off
Quantum switch	Coherent control of channel order	Control/path qubit, coherent switching, interference, port readout, feed-forward	Conditional exact recovery for the selected Pauli sector without redundant encoding; success probability $Q_- = pq$ (or Q_{--})

VI. EXPERIMENTAL FEASIBILITY ON A PHOTONIC PLATFORM

The quantum-switch-assisted QFI teleportation protocol proposed in this work is compatible with existing linear-optical technology. Since standard quantum teleportation has been demonstrated on photonic platforms [2]. The additional requirement for our protocol is the coherent control of two alternative channel sequences, i.e., the quantum switch. A photonic implementation is natural because the polarization and spatial-mode degrees of freedom of a single photon can serve as the target and control qubits, respectively [47, 49, 50].

Figure 8 gives a complete module-level layout. We assign the entangled-photon source and quantum-switch interferometer to the central node Charlie, the input-state preparation and Bell-state measurement (BSM) to Alice, and the conditional correction and tomography to Bob. Charlie generates a polarization-entangled pair $|\Phi^+\rangle_{AB}$ by spontaneous parametric down-conversion (SPDC) in a barium borate (BBO) crystal pumped by laser pulses. Photon A is sent to Alice. The polarization of photon B is sent to Bob through the switched channel, while its spatial mode is the control qubit, a natural photonic encoding used in quantum-switch experiments.

At beam splitter 1 (BS1), photon B is coherently divided between the two paths that implement $\mathcal{E}_2 \circ \mathcal{E}_1$ and $\mathcal{E}_1 \circ \mathcal{E}_2$. The two paths are recombined at a second beam splitter (BS2), which interferometrically recombines the paths and effectively measures the control qubit in the basis $\{|+\rangle, |-\rangle\}$. Such a measurement projects the target polarization state onto the commuting or anti-commuting contributions of the Pauli error trajectories. Both measurement results may be retained as a classical label for the outcome-resolved QFI of Eq. (27); alternatively, the $|-\rangle$ port can herald the exactly correctable branch of a binary channel pair.

The stochastic Pauli maps can be implemented by applying I or the selected Pauli rotation with calibrated probabilities, using synchronized electro-optic polarization modulators or time-multiplexed wave-plate settings. X and Z are obtained with suitable half-wave-plate orientations, while Y is obtained with a calibrated QWP–HWP–QWP sequence.

At Alice, the unknown input photon and photon A overlap on the explicitly shown 50:50 beam splitter; temporal, spectral, and polarization indistinguishability at this beam splitter produces the Hong–Ou–Mandel interference required for a photonic BSM. The two output modes are analyzed by QWP–HWP–PBS stages and single-photon detectors. With passive linear optics and no auxiliary photons, at most two of the four polarization Bell states are unambiguously identified, so the intrinsic BSM success probability satisfies $\eta_{\mathrm{BSM}} \leq 1/2$. Alice sends the identified Bell outcome to Bob. Bob also records the BS2 output port, applies the corresponding correction, and reconstructs the teleported polarization state with QWP–HWP–PBS tomography and two detectors.

The useful heralded count rate scales schematically as

$$R_{\mathrm{use}} \simeq R_{\mathrm{trial}}\, T_A T_B\, \eta_{\mathrm{sw}} \eta_{\mathrm{BSM}} \eta_{\mathrm{det}}\, Q_{\mathrm{sel}}, \tag{55}$$

where T_A and T_B collect transmission, coupling, and path-dependent loss, η_{sw} includes switch visibility and port-routing efficiency, η_{det} collects the required detection efficiencies, and $Q_{\mathrm{sel}} = pq$ for the single-switch $|-\rangle$ branch. For two independent identical arms, $Q_{\mathrm{sel}} = (pq)^2$ for $|--\rangle$. Thus, unit conditional QFI does not imply a unit-rate protocol. Finite interference visibility causes leakage between the commutator and anti-commutator sectors; unequal path loss changes the conditional trajectory weights; multipair emission, detector dark counts, mode mismatch, and feed-forward latency further reduce the measured advantage.

For the dual-switch configuration, two independent control qubits are introduced to coherently manipulate

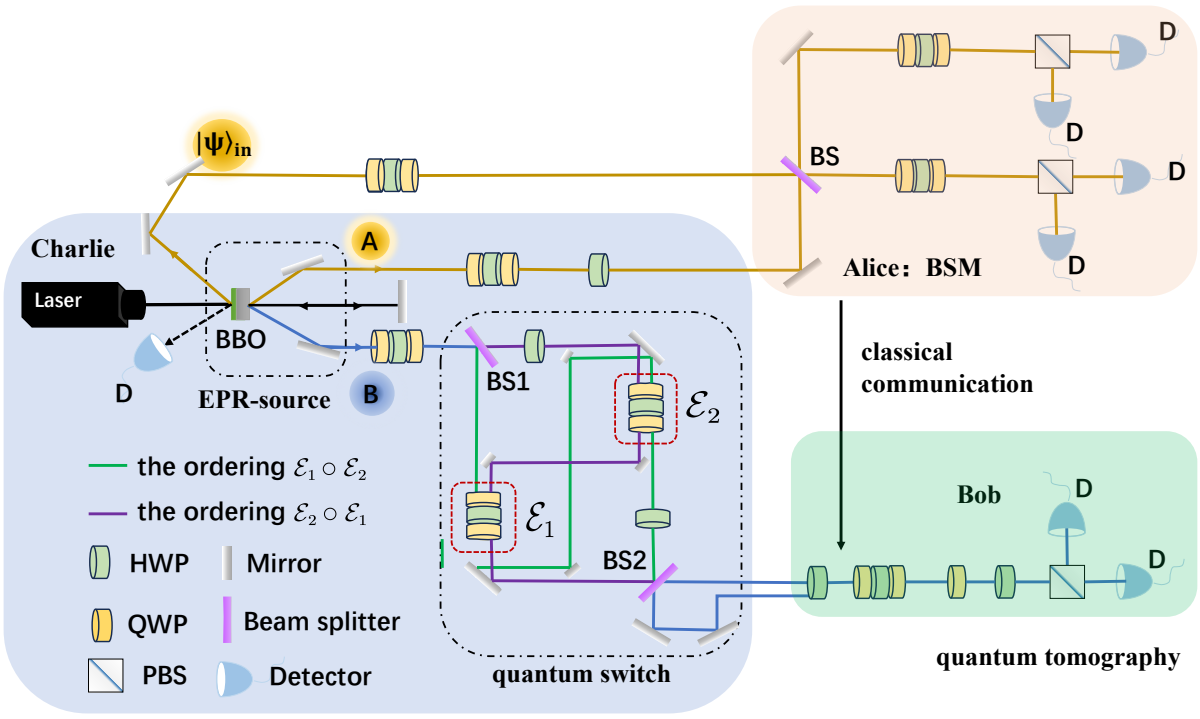


FIG. 8: Experimental proposal. Charlie owns the SPDC entangled-pair source and the phase-stabilized quantum switch. BS1 prepares the spatial control; the solid green path realizes $\mathcal{E}_1$ followed by $\mathcal{E}_2$, the solid purple path realizes the reverse order, and BS2 resolves the $|+\rangle$ and $|-\rangle$ output ports. Alice overlaps the unknown input photon and photon A on a 50:50 beam splitter to produce Hong–Ou–Mandel interference; QWP–HWP–PBS analyzers and detector pairs implement the polarization-resolved BSM. Bob actively routes the control ports and measures the output with QWP–HWP–PBS tomography. Orange and blue denote the photon-A/BSM and photon-B paths, respectively. HWP: half-wave plate; QWP: quarter-wave plate; PBS: polarizing beam splitter; BS: 50:50 beam splitter; D: single-photon detector.

the two channel pairs. Experimentally, this can be achieved by extending the single-switch interferometric architecture with an additional path-control system. The joint measurement of the two control qubits allows the extraction of the conditional branches $|{+}{+}\rangle$, $|{+}{-}\rangle$, $|{-}{+}\rangle$, and $|{-}{-}\rangle$, which correspond to the four causal configurations analyzed in this work. Overall, the proposed protocol is compatible with existing photonic quantum information technologies. Recent experimental demonstrations of ICO-enhanced quantum metrology on photonic platforms provide a direct technological pathway toward verifying this work [67, 83].

VII. CONCLUSIONS

We have investigated the teleportation of phase QFI through sequential Pauli channels under fixed, single-switch, and dual-switch causal structures. Measuring the path control separates commuting and anti-commuting Pauli trajectories. For each binary pair $X+Y$, $X+Z$, and $Y+Z$, the nonzero $|-\rangle$ sector contains one known effective Pauli operation. Its normalized state already has the ideal QFI by unitary invariance, while a parameter-independent feed-forward correction restores the ideal state and standard measurement basis. For two independent noisy arms, the dual-switch result is the corresponding tensor-product construction and the $|--\rangle$ branch is corrected arm by arm. We attribute the underlying mechanism not to a reduction in the physical noise strength but to the reorganization between causal trajectories, a causal-reorganization that factorizes error paths according to their commutation relations.

We emphasize that the QFI enhancement demonstrated here is conditional: it relies on post-selecting specific measurement outcomes of the control qubit(s). In an unconditional setting, e.g., without access to the control measurement results, the advantage disappears, since the four branches average to the fixed-order result. The observed QFI recovery is therefore a consequence of causal-reorganization-assisted error-path factorization, not a cancellation of environmental decoherence. On the other hand, the present analysis is restricted to independent single-qubit Pauli channels. Therefore, these conclusions cannot be directly generalized to the case of correlated Pauli noise, because the error-trajectories under

correlated noise may not be strictly distinguishable.

Potential uses include distributing phase- or frequency-encoded probes between remote sensors, protecting polarization-encoded reference frames and interferometric signals across segmented links, and supplying tagged metrological entanglement to network nodes whose local channels are well approximated by calibrated binary Pauli maps. Practical deployment requires a coherent and phase-stable superposition of channel orders, high-visibility mode matching at both the switch and Bell-measurement beam splitters, low and balanced optical loss, efficient port-resolved control measurement, fast classical feed-forward, and careful accounting of post-selection. Passive linear-optical BSM efficiency, multi-pair emission, detector inefficiency, and the $Q_{-} = pq$ [or $Q_{--} = (pq)^2$] branch probability directly constrain the useful count rate; stabilizing multiple switches is an additional scalability challenge. Future work should incorporate optimizing the information rate rather than conditional QFI alone, and determine whether common-mode or correlated noise can be exploited with a shared-control global switch. Extensions to non-Pauli channels and multiparameter estimation are also open.

ACKNOWLEDGMENTS

X. Xiao is supported by National Natural Science Foundation of China under Grant No. 12265004 and Jiangxi Provincial Natural Science Foundation under Grant No. 20242BAB26010. Y. L. Li is supported by National Natural Science Foundation of China under Grant No. 12365003 and Jiangxi Provincial Key Laboratory of Multidimensional Intelligent Perception and Control of China (No. 2024SSY03161).

DATA AVAILABILITY

The data are available from the authors upon reasonable request.

Appendix A: Details of the four branches of Eqs. (50) and (51)

In this appendix, we give the explicit output states and QFIs obtained by Bob for the four joint outcomes of the two control qubits. Conditional expressions are understood only where the corresponding $Q_{\mu\nu}$ is nonzero.

First, consider the case in which the two control qubits are projected onto $|{+}{+}\rangle$. The resulting output state at Bob's end is

$$\begin{aligned}\rho_{\text{out}}^{++} =& \frac{1}{Q_{++}}\big(\big\{[(a_0+a_3)(c_0+c_3)+(a_1+a_2)(c_1+c_2)]\alpha^2\\ &+[(a_0+a_3)(c_1+c_2)+(a_1+a_2)(c_0+c_3)]|\beta|^2\big\}|0\rangle\langle 0|\\ &+\big\{[(a_0+a_3)(c_1+c_2)+(a_1+a_2)(c_0+c_3)]\alpha^2\\ &+[(a_0+a_3)(c_0+c_3)+(a_1+a_2)(c_1+c_2)]|\beta|^2\big\}|1\rangle\langle 1|\\ &+\big\{[(a_0-a_3)(c_0-c_3)+(a_1-a_2)(c_1-c_2)]\alpha\beta^\dagger\\ &+[(a_0-a_3)(c_1-c_2)+(a_1-a_2)(c_0-c_3)]\alpha\beta\big\}|0\rangle\langle 1|\\ &+\big\{[(a_0-a_3)(c_1-c_2)+(a_1-a_2)(c_0-c_3)]\alpha\beta^\dagger\\ &+[(a_0-a_3)(c_0-c_3)+(a_1-a_2)(c_1-c_2)]\alpha\beta\big\}|1\rangle\langle 0|\big).\end{aligned} \tag{A1}$$

Applying Eq. (4), we obtain the corresponding QFI as

$$\mathcal{F}^{++} = \begin{cases} \frac{M_{++}}{Q_{++}^2}, & \text{if } |\boldsymbol{\omega}_{++}| = 1,\\ \frac{M_{++}}{Q_{++}^2} + \frac{(B_{++}^2 - A_{++}^2)^2 \sin^4\theta \sin^2 2\phi}{4(Q_{++})^4\left(1-|\boldsymbol{\omega}_{++}|^2\right)}, & \text{if } |\boldsymbol{\omega}_{++}| < 1, \end{cases} \tag{A2}$$

Here $M_{++} = \sin^2\theta(A_{++}^2\sin^2\phi + B_{++}^2\cos^2\phi)$, $|\boldsymbol{\omega}_{++}| = \frac{1}{Q^{++}}\sqrt{N_{++}+C_{++}^2\cos^2\theta}$, $N_{++} = \sin^2\theta(A_{++}^2\cos^2\phi + B_{++}^2\sin^2\phi)$, $A_{++} = (a_0+a_1-a_2-a_3)(c_0+c_1-c_2-c_3)$, $B_{++} = (a_0-a_1+a_2-a_3)(c_0-c_1+c_2-c_3)$, and $C_{++} = (a_0-a_1-a_2+a_3)(c_0-c_1-c_2+c_3)$. Similarly, for the other three control-basis states $|{+}{-}\rangle$, $|{-}{+}\rangle$, and $|{-}{-}\rangle$, the respective output states are as follows.

For the $|{+}{-}\rangle$ outcome,

$$\begin{aligned}\rho_{\text{out}}^{+-} =&\frac{1}{Q_{+-}}\big(\big\{[(a_0+a_3)(d_0+d_3)+(a_1+a_2)(d_1+d_2)]\alpha^2\\ &+[(a_0+a_3)(d_1+d_2)+(a_1+a_2)(d_0+d_3)]|\beta|^2\big\}|0\rangle\langle 0|\\ &+\big\{[(a_0+a_3)(d_1+d_2)+(a_1+a_2)(d_0+d_3)]\alpha^2\\ &+[(a_0+a_3)(d_0+d_3)+(a_1+a_2)(d_1+d_2)]|\beta|^2\big\}|1\rangle\langle 1|\\ &+\big\{[(a_0-a_3)(d_0-d_3)+(a_1-a_2)(d_1-d_2)]\alpha\beta^\dagger\\ &+[(a_0-a_3)(d_1-d_2)+(a_1-a_2)(d_0-d_3)]\alpha\beta\big\}|0\rangle\langle 1|\\ &+\big\{[(a_0-a_3)(d_1-d_2)+(a_1-a_2)(d_0-d_3)]\alpha\beta^\dagger\\ &+[(a_0-a_3)(d_0-d_3)+(a_1-a_2)(d_1-d_2)]\alpha\beta\big\}|1\rangle\langle 0|\big),\end{aligned} \tag{A3}$$

The associated QFI is

$$\mathcal{F}^{+-}=\begin{cases}\frac{M_{+-}}{Q_{+-}^2}, & \text{if } |\boldsymbol{\omega}_{+-}|=1,\\ \frac{M_{+-}}{Q_{+-}^2}+\frac{(B_{+-}^2-A_{+-}^2)^2\sin^4\theta\sin^2 2\phi}{4(Q_{+-})^4\left(1-|\boldsymbol{\omega}_{+-}|^2\right)}, & \text{if } |\boldsymbol{\omega}_{+-}|<1,\end{cases} \tag{A4}$$

Here $M_{+-}=\sin^2\theta(A_{+-}^2\sin^2\phi+B_{+-}^2\cos^2\phi)$, $|\boldsymbol{\omega}_{+-}|=\frac{1}{Q^{+-}}\sqrt{N_{+-}+C_{+-}^2\cos^2\theta}$, $N_{+-}=\sin^2\theta(A_{+-}^2\cos^2\phi+B_{+-}^2\sin^2\phi)$, $A_{+-}=(a_0+a_1-a_2-a_3)(d_1-d_2-d_3)$, $B_{+-}=(a_0-a_1+a_2-a_3)(-d_1+d_2-d_3)$, and $C_{+-}=(a_0-a_1-a_2+a_3)(-d_1-d_2+d_3)$.

For the $|-+\rangle$ outcome,

$$\begin{aligned}\rho_{\text{out}}^{-+} =&\frac{1}{Q_{-+}}\big(\big\{[(b_0+b_3)(c_0+c_3)+(b_1+b_2)(c_1+c_2)]\alpha^2\\ &+[(b_0+b_3)(c_1+c_2)+(b_1+b_2)(c_0+c_3)]|\beta|^2\big\}|0\rangle\langle 0|\\ &+\big\{[(b_0+b_3)(c_1+c_2)+(b_1+b_2)(c_0+c_3)]\alpha^2\\ &+[(b_0+b_3)(c_0+c_3)+(b_1+b_2)(c_1+c_2)]|\beta|^2\big\}|1\rangle\langle 1|\\ &+\big\{[(b_0-b_3)(c_0-c_3)+(b_1-b_2)(c_1-c_2)]\alpha\beta^\dagger\\ &+[(b_0-b_3)(c_1-c_2)+(b_1-b_2)(c_0-c_3)]\alpha\beta\big\}|0\rangle\langle 1|\\ &+\big\{[(b_0-b_3)(c_1-c_2)+(b_1-b_2)(c_0-c_3)]\alpha\beta^\dagger\\ &+[(b_0-b_3)(c_0-c_3)+(b_1-b_2)(c_1-c_2)]\alpha\beta\big\}|1\rangle\langle 0|\big),\end{aligned} \tag{A5}$$

yielding the QFI expression,

$$\mathcal{F}^{-+}=\begin{cases}\frac{M_{-+}}{Q_{-+}^2}, & \text{if } |\boldsymbol{\omega}_{-+}|=1,\\ \frac{M_{-+}}{Q_{-+}^2}+\frac{(B_{-+}^2-A_{-+}^2)^2\sin^4\theta\sin^2 2\phi}{4(Q_{-+})^4\left(1-|\boldsymbol{\omega}_{-+}|^2\right)}, & \text{if } |\boldsymbol{\omega}_{-+}|<1,\end{cases} \tag{A6}$$

Here $M_{-+}=\sin^2\theta(A_{-+}^2\sin^2\phi+B_{-+}^2\cos^2\phi)$, $|\boldsymbol{\omega}_{-+}|=\frac{1}{Q^{-+}}\sqrt{N_{-+}+C_{-+}^2\cos^2\theta}$, $N_{-+}=\sin^2\theta(A_{-+}^2\cos^2\phi+B_{-+}^2\sin^2\phi)$, $A_{-+}=(b_1-b_2-b_3)(c_0+c_1-c_2-c_3)$, $B_{-+}=(-b_1+b_2-b_3)(c_0-c_1+c_2-c_3)$, and $C_{-+}=(-b_1-b_2+b_3)(c_0-c_1-c_2+c_3)$.

Finally, for the $|--\rangle$ outcome, the output state reads,

$$\begin{aligned}\rho_{\text{out}}^{--} =&\frac{1}{Q_{--}}\big(\big\{[(b_0+b_3)(d_0+d_3)+(b_1+b_2)(d_1+d_2)]\alpha^2\\ &+[(b_0+b_3)(d_1+d_2)+(b_1+b_2)(d_0+d_3)]|\beta|^2\big\}|0\rangle\langle 0|\\ &+\big\{[(b_0+b_3)(d_1+d_2)+(b_1+b_2)(d_0+d_3)]\alpha^2\\ &+[(b_0+b_3)(d_0+d_3)+(b_1+b_2)(d_1+d_2)]|\beta|^2\big\}|1\rangle\langle 1|\\ &+\big\{[(b_0-b_3)(d_0-d_3)+(b_1-b_2)(d_1-d_2)]\alpha\beta^\dagger\\ &+[(b_0-b_3)(d_1-d_2)+(b_1-b_2)(d_0-d_3)]\alpha\beta\big\}|0\rangle\langle 1|\\ &+\big\{[(b_0-b_3)(d_1-d_2)+(b_1-b_2)(d_0-d_3)]\alpha\beta^\dagger\\ &+[(b_0-b_3)(d_0-d_3)+(b_1-b_2)(d_1-d_2)]\alpha\beta\big\}|1\rangle\langle 0|\big).\end{aligned} \tag{A7}$$

Consequently, the QFI takes the form,

$$\mathcal{F}^{--}=\begin{cases}\frac{M_{--}}{Q_{--}^2}, & \text{if } |\boldsymbol{\omega}_{--}|=1,\\ \frac{M_{--}}{Q_{--}^2}+\frac{(B_{--}^2-A_{--}^2)^2\sin^4\theta\sin^2 2\phi}{4(Q_{--})^4\left(1-|\boldsymbol{\omega}_{--}|^2\right)}, & \text{if } |\boldsymbol{\omega}_{--}|<1,\end{cases} \tag{A8}$$

Here $M_{--}=\sin^2\theta(A_{--}^2\sin^2\phi+B_{--}^2\cos^2\phi)$, $|\boldsymbol{\omega}_{--}|=\frac{1}{Q^{--}}\sqrt{N_{--}+C_{--}^2\cos^2\theta}$, $N_{--}=\sin^2\theta(A_{--}^2\cos^2\phi+B_{--}^2\sin^2\phi)$, $A_{--}=(b_1-b_2-b_3)(d_1-d_2-d_3)$, $B_{--}=(-b_1+b_2-b_3)(-d_1+d_2-d_3)$, and $C_{--}=(-b_1-b_2+b_3)(-d_1-d_2+d_3)$.

[1] Bennett C H, Brassard G, Crépeau C, Jozsa R, Peres A and Wootters W K 1993 *Phys. Rev. Lett.* **70** 1895
[2] Bouwmeester D, Pan J W, Mattle K, Eibl M, Weinfurter H and Zeilinger A 1997 *Nature* **390** 575
[3] Pirandola S, Eisert J, Weedbrook C, Furusawa A and Braunstein S L 2015 *Nat. Photon.* **9** 641
[4] Hu X M, Guo Y, Liu B H, Li C F and Guo G C 2023 *Nat. Rev. Phys.* **5** 339
[5] Giovannetti V, Lloyd S and Maccone L 2006 *Phys. Rev. Lett.* **96** 010401
[6] Giovannetti V, Lloyd S and Maccone L 2011 *Nat. Photon.* **5** 222
[7] Liu J, Yuan H, Lu X M and Wang X 2020 *J. Phys. A: Math. Theor.* **53** 023001
[8] Helstrom C W 1969 *J. Stat. Phys.* **1** 231
[9] Scandi M, Abiuso P, Surace J and De Santis D 2025 *Rep. Prog. Phys.* **88** 076001
[10] Tóth G and Apellaniz I 2014 *J. Phys. A: Math. Theor.* **47** 424006
[11] Xiang G Y and Guo G C 2013 *Chin. Phys. B* **22** 110601
[12] Zhang Z and Zhuang Q 2021 *Quantum Sci. Technol.* **6** 043001
[13] Guo X, Breum C R, Borregaard J, Izumi S, Larsen M V, Gehring T, Christandl M, Neergaard-Nielsen J S and Andersen U L 2020 *Nat. Phys.* **16** 281
[14] Liu L Z, Zhang Y Z, Li Z D, Zhang R, Yin X F, Fei Y Y, Li L, Liu N L, Xu F, Chen Y A and Pan J W 2021 *Nat. Photon.* **15** 137
[15] Basset M G, Setzpfandt F, Steinlechner F, Beckert E, Pertsch T and Gräfe M 2019 *Laser Photonics Rev.* **13** 1900097
[16] Defienne H, Bowen W P, Chekhova M, Lemos G B, Oron D, Ramelow S, Treps N and Faccio D 2024 *Nat. Photon.* **18** 1024
[17] Schnabel R, Mavalvala N, McClelland D E and Lam P K 2010 *Nat. Commun.* **1** 121
[18] Tse M, Yu H, Kijbunchoo N, Fernandez-Galiana A, Dupej P, Barsotti L, Blair C D, Brown D D, Dwyer S E, *et al* 2019 *Phys. Rev. Lett.* **123** 231107
[19] Breuer H P and Petruccione F 2002 *The Theory of Open Quantum Systems* (New York: Oxford University Press)
[20] Escher B M, de Matos Filho R L and Davidovich L 2011 *Braz. J. Phys.* **41** 229
[21] Nichols R, Bromley T R, Correa L A and Adesso G 2016 *Phys. Rev. A* **94** 042101
[22] Viola L, Knill E and Lloyd S 1999 *Phys. Rev. Lett.* **82** 2417
[23] Lidar D A, Chuang I L and Whaley K B 1998 *Phys. Rev. Lett.* **81** 2594
[24] Maniscalco S, Francica F, Zaffino R L, Lo Gullo N and Plastina F 2008 *Phys. Rev. Lett.* **100** 090503
[25] Korotkov A N and Keane K 2010 *Phys. Rev. A* **81** 040103
[26] Lidar D A and Brun T A 2013 *Quantum Error Correction* (Cambridge: Cambridge University Press)
[27] Bai S Y and An J H 2023 *Phys. Rev. Lett.* **131** 050801
[28] Tan Q S, Huang Y, Yin X, Kuang L M and Wang X 2013 *Phys. Rev. A* **87** 032102
[29] Sekatski P, Skotiniotis M and Dür W 2016 *New J. Phys.* **18** 073034
[30] Louzon D, Genov G T, Staudenmaier N, Frank F, Lang J, Markham M L, Retzker A and Jelezko F 2025 *Phys. Rev. Lett.* **134** 120802
[31] Dür W, Skotiniotis M, Fröwis F and Kraus B 2014 *Phys. Rev. Lett.* **112** 080801
[32] Zhou S, Zhang M, Preskill J and Jiang L 2018 *Nat. Commun.* **9** 78
[33] Kim Y S, Lee J C, Kwon O and Kim Y H 2012 *Nat. Phys.* **8** 117
[34] Xiao X and Li Y L 2013 *Eur. Phys. J. D* **67** 204
[35] Xiao X, Yao Y, Xie Y M, Wang X H and Li Y L 2016 *Quantum Inf. Process.* **15** 3881
[36] Xiao X, Yao Y, Zhong W J, Li Y L and Xie Y M 2016 *Phys. Rev. A* **93** 012307
[37] Li Y L, Sun F, Yang J and Xiao X 2021 *Quantum Inf. Process.* **20** 55
[38] Li Y L, Zu C J and Wei D M 2019 *Quantum Inf. Process.* **18** 2
[39] Xiao X, Yao Y, Li Y L and Xie Y M 2020 *Eur. Phys. J. Plus* **135** 79
[40] Harraz S, Cong S and Nieto J J 2022 *IEEE Commun. Lett.* **26** 528
[41] Terhal B M 2015 *Rev. Mod. Phys.* **87** 307
[42] Flammia S T and Wallman J J 2020 *ACM Trans. Quantum Comput.* **1** 1
[43] Wang K, Wang X, Zhan X, Bian Z, Li J, Sanders B C and Xue P 2018 *Phys. Rev. A* **97** 042112
[44] Lee D, Lee J, Hong S, Lim H T, Cho Y W, Han S W, Shin H, Rehman J and Kim Y S 2022 *Optica* **9** 88
[45] Ware M, Ribeill G, Ristè D, Ryan C A, Johnson B and da Silva M P 2021 *Phys. Rev. A* **103** 042604
[46] Van den Berg E and Wocjan P 2024 *Quantum* **8** 1556
[47] Procopio L M, Moqanaki A, Araújo M, Costa F, Alonso Calafell I, Dowd E G, Hamel D R, Rozema L A, Brukner Č and Walther P 2015 *Nat. Commun.* **6** 7913

[48] Araújo M, Feix A, Navascués M and Brukner Č 2017 *Quantum* **1** 10

[49] Rubino G, Rozema L A, Feix A, Araújo M, Zeuner J M, Procopio L M, Brukner Č and Walther P 2017 *Sci. Adv.* **3** e1602589

[50] Rozema L A, Strömberg T, Cao H, Guo Y, Liu B H and Walther P 2024 *Nat. Rev. Phys.* **6** 483

[51] Goswami K, Giarmatzi C, Kewming M, Costa F, Branciard C, Romero J and White A G 2018 *Phys. Rev. Lett.* **121** 090503

[52] Caleffi M and Cacciapuoti A S 2020 *IEEE J. Sel. Areas Commun.* **38** 575

[53] Felce D and Vedral V 2020 *Phys. Rev. Lett.* **125** 070603

[54] Guo Y, Hu X M, Hou Z B, Cao H, Cui J M, Liu B H, Huang Y F, Li C F, Guo G C and Chiribella G 2020 *Phys. Rev. Lett.* **124** 030502

[55] Loizeau N and Grinbaum A 2020 *Phys. Rev. A* **101** 012340

[56] Zhu G, Chen Y, Hasegawa Y and Xue P 2023 *Phys. Rev. Lett.* **131** 240401

[57] Costa F, Rubino G, Branciard C, Brukner Č and Quintino M T 2026 arXiv:2606.19438 [quant-ph]

[58] Ebler D, Salek S and Chiribella G 2018 *Phys. Rev. Lett.* **120** 120502

[59] Chandra D, Caleffi M and Cacciapuoti A S 2022 *IEEE Trans. Wirel. Commun.* **21** 3632

[60] Chiribella G, Banik M, Bhattacharya S S, Guha T, Alimuddin M, Roy A, Saha S, Agrawal S and Kar G 2021 *New J. Phys.* **23** 033039

[61] Liu X, Ebler D and Dahlsten O 2022 *Phys. Rev. Lett.* **129** 230604

[62] Li Y L, Mu Z and Xiao X 2025 *Phys. Scr.* **100** 125104

[63] Bavaresco J, Murao M and Quintino M T 2021 *Phys. Rev. Lett.* **127** 200504

[64] Kechrimparis S, Moran J, Karsa A, Lee C and Kwon H 2024 *New J. Phys.* **26** 123030

[65] Ban M 2023 *Phys. Lett. A* **468** 128749

[66] An M, Ru S, Wang Y, Yang Y, Wang F, Zhang P and Li F 2024 *Phys. Rev. A* **109** 012603

[67] Guo Y, Chen Y, Chen G, Hu X M, Huang Y F, Li C F, Guo G C and Liu B H 2025 arXiv:2505.03290 [quant-ph]

[68] Xu H, Deng X, Zheng Z, Xiao T and Zeng G 2026 arXiv:2601.01404 [quant-ph]

[69] Dey I and Marchetti N 2023 arXiv:2303.10683 [quant-ph]

[70] Liu W Q and Wei H R 2025 *Phys. Rev. Appl.* **23** 014064

[71] Helstrom C W 1976 *Quantum Detection and Estimation Theory* (Academic Press)

[72] Knysh S, Smelyanskiy V N and Durkin G A 2011 *Phys. Rev. A* **83** 021804

[73] Liu J, Jing X and Wang X 2013 *Phys. Rev. A* **88** 042316

[74] Watanabe Y, Sagawa T and Ueda M 2010 *Phys. Rev. Lett.* **104** 020401

[75] Zhong W, Sun Z, Ma J, Wang X and Nori F 2013 *Phys. Rev. A* **87** 022337

[76] Chiribella G, D'Ariano G M, Perinotti P and Valiron B 2013 *Phys. Rev. A* **88** 022318

[77] Salek S, Ebler D and Chiribella G 2018 arXiv:1809.06655 [quant-ph]

[78] Nielsen M A and Chuang I L 2010 *Quantum Computation and Quantum Information* (Cambridge: Cambridge University Press)

[79] Czegledi C B, Karlsson M, Agrell E and Johannisson P 2016 *Sci. Rep.* **6** 21217

[80] Kucera S, Haen C, Arenskötter E, Bauer T, Meiers J, Schäfer M, Boland R, Yahyapour M, Lessing M, Holzwarth R, Becher C and Eschner J 2024 *npj Quantum Inf.* **10** 88

[81] Brodsky M, George E C, Antonelli C and Shtaif M 2011 *Opt. Lett.* **36** 43

[82] Jarzyna M and Demkowicz-Dobrzański R 2015 *New J. Phys.* **17** 013010

[83] Yin P, Zhao X, Yang Y, Guo Y, Zhang W H, Li G C, Han Y J, Liu B H, Xu J S, Chiribella G, Chen G, Li C F and Guo G C 2023 arXiv:2303.17223 [quant-ph]